UNIVERSITY OF CALIFORNIA
RIVERSIDE

Control of Néel Vector in Antiferromagnets

A Dissertation submitted in partial satisfaction
of the requirements for the degree of

Doctor of Philosophy

in

Electrical Engineering

by

In Jun Park

December 2020

Dissertation Committee:

Dr. Roger K. Lake, Chairperson
Dr. Alexander Balandin
Dr. Ran Cheng

The Dissertation of In Jun Park is approved:

Committee Chairperson

University of California, Riverside

Acknowledgments

First of all, I want to thank my advisor and mentor, Professor Roger K. Lake, for accepting me as his student. During my PhD, I have learned a lot from him about material science engineering, condensed matter physics, and scientific writings for publications and proposals. He always gave me fruitful advices and comments whenever I was struggling with my projects. Without his constant support, I would not be here. I acknowledge my collaborators, Dr. Ted Lee and Prof. Greg P. Carman from UCLA for their insightful comments and discussions.

Special thanks to my current labmates in LATTE lab, Rakibul Karim Akanda, Topojit Debnath, Yuhang Liu, Sohee Kwon, Hector Gomez, as well as my former colleagues and friends Dr. Chenyang Li, Dr. Nima Djavid, Dr. Protik Das, and Dr. Bishwajit Debnath, for their help and support with many ideas, collaborative projects and enjoyable discussions.

On the personal side, I would like to acknowledge my family and friends for their continuous support over the past few years. I am thankful to my parents for their guidance and support for my higher education. I cannot imagine myself here today pursuing my PhD without their dedication, unconditional love, and true support for me.

The text of this dissertation, in part or in full, is a reprint of the material as it appears in the following journal:

- Applied Physics Letters [1] [2019], with the permission of AIP Publishing
- Physical Review B [2] [2020]. Amerian Physical Society

The co-author Roger K. Lake, listed in the above publications directed and supervised the research which forms the basis for this dissertation. The remaining co-authors listed provided technical expertise and support as collaborators. This work was supported as part of Spins and Heat in Nanoscale Electronic Systems (SHINES) an Energy Frontier Research Center funded by the U.S. Department of Energy, Office of Science, Basic Energy Sciences under Award #DE-SC0012670. The numerical simulation used the Extreme Science and Engineering Discovery Environment (XSEDE) [3], which is supported by National Science Foundation Grant No. ACI-1548562 and allocation ID TG-DMR130081.

To my family

ABSTRACT OF THE DISSERTATION

Control of Néel Vector in Antiferromagnets

by

In Jun Park

Doctor of Philosophy, Graduate Program in Electrical Engineering
University of California, Riverside, December 2020
Dr. Roger K. Lake, Chairperson

Control of the Néel vector in antiferromagnetic materials is one of the challenges preventing their use as active device components. Several methods have been investigated such as exchange bias, electric current, and spin injection, but little is known about strain-mediated anisotropy. This study of the antiferromagnetic $L1_0$-type MnX alloys MnIr, MnRh, MnNi, MnPd, and MnPt shows that a small amount of strain effectively rotates the direction of the Néel vector by 90° for all of the materials. For MnIr, MnRh, MnNi, and MnPd, the Néel vector rotates within the basal plane. For MnPt, the Néel vector rotates from out-of-plane to in-plane under tensile strain. The effectiveness of strain control is quantified by a metric of efficiency and by direct calculation of the magnetostriction coefficients. The values of the magnetostriction coefficients are comparable with those from ferromagnetic materials. These results indicate that strain is a mechanism that can be exploited for control of the Néel vectors in this family of antiferromagnets.

CrSb is a layered antiferromagnet (AFM) with perpendicular magnetic anisotropy, a high Néel temperature, and large spin-orbit coupling (SOC), which makes it interesting for

AFM spintronic applications. To elucidate the various mechanisms of Néel vector control, the effects of strain, band filling, and electric field on the magnetic anisotropy energy (MAE) of bulk and thin-film CrSb are determined and analysed using density functional theory. The MAE of the bulk crystal is large (1.2 meV per unit cell). Due to the significant ionic nature of the Cr-Sb bond, finite slabs are strongly affected by end termination. Truncation of the bulk crystal to a thin film with one surface terminated with Cr and the other surface terminated with Sb breaks inversion symmetry, creates a large charge dipole and average electric field across the film, and breaks spin degeneracy, such that the thin film becomes a ferrimagnet. The MAE is reduced such that its sign can be switched with realistic strain, and the large SOC gives rise to an intrinsic voltage controlled magnetic anisotropy (VCMA). A slab terminated on both faces with Cr remains a compensated AFM, but with the compensation occurring nonlocally between mirror symmetric Cr pairs. In-plane alignment of the moments is preferred, the magnitude of the MAE remains large, similar to that of the bulk, and it is relatively insensitive to filling.

Contents

List of Figures

List of Tables

Chapter 1

Rationale

1.1 Objectives

Since the metal-oxide-semiconductor field effect transistor (MOSFET) was invented, conventional electronics has exponentially improved. The density of transistors on integrated circuits has doubled every two years, and this trend is known as Moore's law. The increased density is the result of scaling, in which the the dimensions of MOSFETs are reduced. However, continued scaling to nanometer dimensions is hindered by short channel effects and quantum mechanical tunneling, and now scaling is reaching its physical limits due to quantum effects. The field of study of spintronics or spin electronics [4, 5] has been a promising direction increasing memory density and reducing power since the discovery of giant magnetoresistance (GMR) [6, 7]. The field aims to control electrons and spins in solid state systems. Ferromagnetic (FM) materials have been widely used in the vast majority of studies. In FM materials, the spin on each lattice site is parallel to that on the neighboring lattice sites for temperatures below the Curie temperature (T_c), so that there exists

a net magnetization. The magnetization gives rise to magnetic fields near the materials, which allows them to be easily detected. Moreover, the spins in FM materials can be manipulated by an external magnetic field, exchange bias, electric current, electric field, and strain. A different class of magnetic materials, antiferromagnets, was discovered by Louis Néel in 1940's. In collinear antiferromagnetic (AFM) materials, the magnetic moment of one sub-lattice is anti-parallel to that of the neighboring one so that the net magnetization is zero below the Néel temperature (T_N). Since there is zero net magnetization, there is an absence of stray fields, which allows deep scaling of AFM spintronic devices without suffering from cross-talk. Moreover, in comparison to FM materials, AFM materials exhibit ultrafast dynamics [8, 9] and are able to provide large magnetotransport effects compared to FM materials. Due to the appealing properties of AFM materials, extensive research has been conducted on them, creating a new sub-field called AFM spintronics [8, 10], aimed at complementing or replacing FM materials in the active region of spintronic devices with AFM materials. One of the challenges in AFM spintronics is to control the Néel vector. There are several methods to control the Néel vector, such as with exchange bias, electric current, and electric field. Although most of researchers focus on the switching the Néel vector by electric current, using electric field has advantages in terms of power consumption [11] and switching speed [12]. For future usage, it is important for AFM materials to be compatible with CMOS technology. On-chip operation requires high Néel temperatures. AFM materials discussed in this thesis, such as MnIr, MnRh, MnNi, MnPd, MnPt, and CrSb, have high Néel temperatures [13–16], which makes them suitable candidates for on-chip applications.

1.2 Organization

The rest of the dissertation is organized as follows. Chapter 2 investigates the magnetic anisotropy energy in Mn-based antiferromagnets as a function of strain. Chapter 3 analyzes how filling, strain, and electric field affect the magnetic anisotropy energy in the antiferromagnetic CrSb. In Appendix A, the calculated lattice constants and magnetoelastic anisotropy constants are plotted. Also, the determination of Young's moduli of MnX alloys is discussed. Appendix B privides Python scripts for calculations of the magnetic anisotropy energy as a function of applied strain and electric field. In Appendix C, the calculation of Bader charge, planar averaged Hartree potential, and charge density is discussed.

Chapter 2

Strain control of the Néel vector in Mn-based antiferromagnets

2.1 Introduction

There has been a rapidly increasing interest in the use of antiferromagnetic (AFM) materials for use as active device elements [10, 17, 18]. AFMs are insensitive to parasitic electromagnetic and magnetic interference. The dipolar coupling is minimal, since there is no net magnetic moment. Their lack of macroscopic magnetic fields allows AFM devices and interconnects to be highly scaled with reduced cross talk and insensitivity to geometrical anisotropy effects. AFM resonant frequencies and magnon velocities are several orders of magnitude higher than those in ferromagnetic materials, and these velocities correlate with similarly higher switching speeds [8, 10, 19]. AFM metals and insulators are plentiful, and

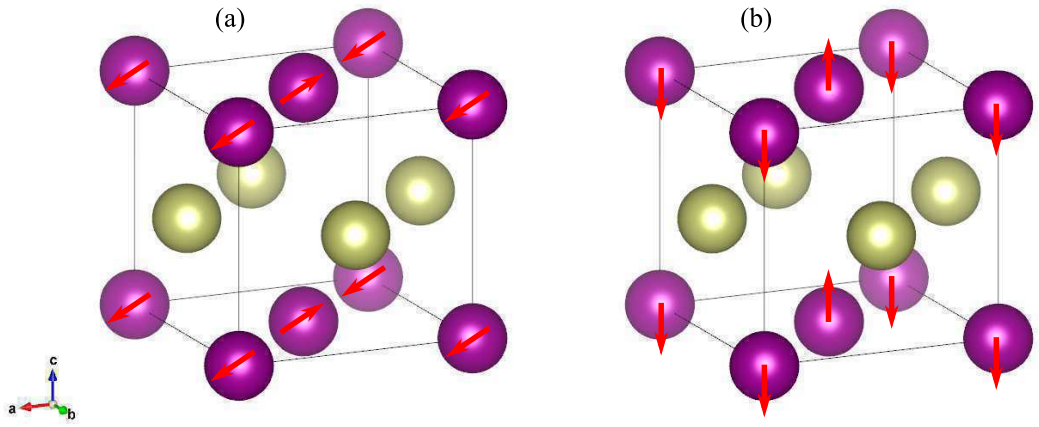

Figure 2.1: Antiferromagnetic $L1_0$-type Mn alloy structures. Mn atoms are the purple spheres with the spin vectors, and the gold spheres indicate the Ir, Rh, Ni, Pd, or Pt atoms. (a) In-plane equilibrium spin texture of MnIr, MnRh, MnNi, and MnPd. (b) Out-of-plane equilibrium spin texture of MnPt.

many have Néel temperatures well above room temperature, a requirement for compatibility with on-chip temperatures in current Si integrated circuits.

The high Néel temperatures of the Mn-based equiatomic alloys such as MnIr, MnRh, MnNi, MnPd, and MnPt make them suitable candidates for on-chip applications [17]. Extensive research has been conducted on the electronic [14, 20–23], magnetic [14, 15, 20, 23], and elastic properties [24, 25] of these materials. The spins on the Mn atoms are antiferromagnetically coupled with each other in the basal plane, and each plane is coupled ferromagnetically as shown in Fig. 3.1.

The positive attributes of speed, scaling, and robustness to stray fields are accompanied by the challenges of manipulating and detecting the antiferromagnetic states. There are several methods to control the magnetic properties of AFM materials such as

with exchange bias [17], the use of electric current [26], and strain induced by a piezoelectric material [27–30]. The recent experimental demonstration of strain control of the Néel vector in MnPt [30], provides timely motivation for a theoretical study of strain-meditated magnetic anisotropy in the MnX AFM materials. Density functional theory (DFT) is used to analyze the effect of strain on the magnetic anisotropy. The effectiveness of strain control is quantified by a metric of efficiency and by calculation of the magnetostriction coefficients.

2.2 Method

Table 2.1: Calculated structure and local magnetic moment of the $L1_0$-type MnX alloys in the absence of strain.

	a (Å)	b (Å)	c (Å)	μ_{Mn} (μ_B)
MnIr	3.84	3.84	3.64	2.8
MnRh	3.85	3.85	3.62	3.1
MnNi	3.62	3.62	3.58	3.2
MnPd	3.99	3.99	3.69	3.8
MnPt	3.98	3.98	3.71	3.7

First principles calculations are performed as implemented in the Vienna Ab initio Simulation Package (VASP) [31] to investigate the effect of strain on the magnetic anisotropy of $L1_0$-ordered bulk MnIr, MnRh, MnNi, MnPd, and MnPt. Projector augmented-wave (PAW) potentials [32] and the generalized gradient approximation (GGA) parameterized by Perdew-Burke-Ernzerhof (PBE) were employed [33]. Depending on the materials, different cut-off energies (typically ranging from 420 eV to 450 eV) and k-points grids were used

in order to ensure the total energy converged within 10^{-7} eV per unit cell. The initial equilibrium structure consists of a tetragonal unit cell where the fractional coordinates of Mn atoms are (0, 0, 0) and (0.5, 0.5, 0), and those of the X atoms are (0.5, 0, 0.5) and (0, 0.5, 0.5). Compressive or tensile stress along the a axis is applied to each structure, and the structure is fully relaxed along the b and c axes (biaxially) until all forces on each atom are less than 10^{-4} eVÅ^{-1}. The relaxed lattice constants for each applied strain are shown in Appendix A Fig. A.1. The strain is defined as, strain $= (a - a_0)/a_0 \times 100\%$, where a and a_0 are the lattice constants with and without strain, respectively. With the relaxed structure, the spin-polarized self-consistent calculation is performed to obtain the charge density. Finally, the magnetic anisotropy energies are determined by calculating the total energies for different Néel vector directions including spin orbit coupling. Table 2.1 shows the lattice constants and the magnetic moments of the Mn site in MnX without strain. All of the values are very close to those from previous results [24, 25]. The local magnetic moments of the X site are zero for all materials.

2.3 Results and Discussion

Figures 2.2–2.6 show the differences in the total energies as a function of the strain for MnIr, MnRh, MnNi, MnPd, and MnPt, respectively, where E_{abc} is the ground state energy with the Néel vector along the $[abc]$ direction. The reference energy levels from each figure, which are indicated by the solid black lines, are E_{001} for MnPt and E_{110} for the other materials. The reference energies are the lowest energy state, which means MnIr, MnRh, MnNi, and MnPd have in-plane anisotropy and MnPt has out-of-plane anisotropy without

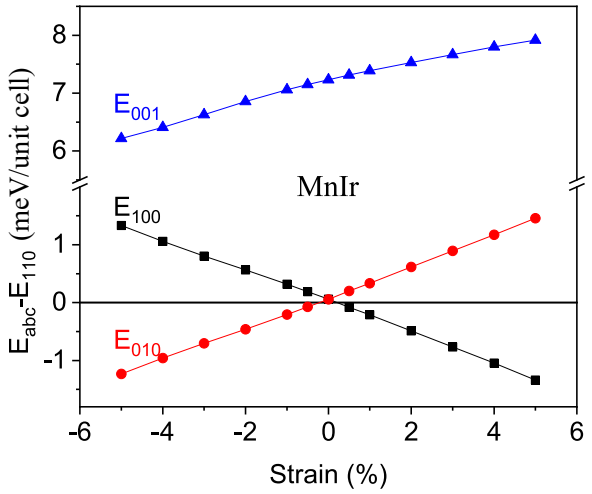

Figure 2.2: MnIr energy differences $E_{abc} - E_{110}$ for the 3 different orientations of the Néel vector as indicated by the labels.

strain. This is consistent with experimental results [15]. To show the energy differences more clearly as the strain changes, the reference level is taken at each value of the applied strain. At zero strain, there is no energy difference between E_{100} and E_{010} because of the symmetry of all of the materials.

Figures 2.2–2.5 show that sweeping the strain from negative (compressive) to positive (tensile) causes a 90° rotation of the Néel vector in the *ab*-plane for the four materials MnIr, MnRh, MnNi, and MnPd. However, the alignment of the Néel vector with compressive or tensile strain depends on the specific material. MnIr and MnRh behave like magnets with a positive magnetostriction coefficient, since tensile strain along [100] causes the Néel vector to align in the [100] direction. On the other hand, MnNi and MnPd behave like

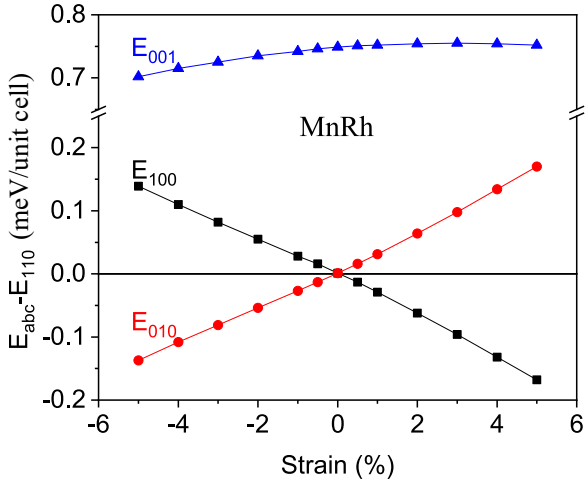

Figure 2.3: MnRh energy differences $E_{abc} - E_{110}$ for the 3 different orientations of the Néel vector as indicated by the labels.

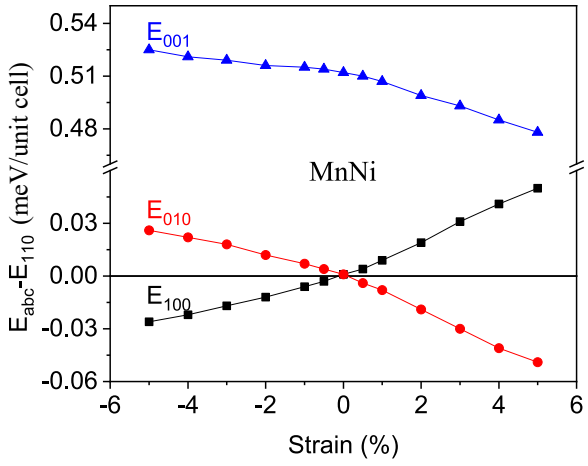

Figure 2.4: MnNi energy differences $E_{abc} - E_{110}$ for the 3 different orientations of the Néel vector as indicated by the labels.

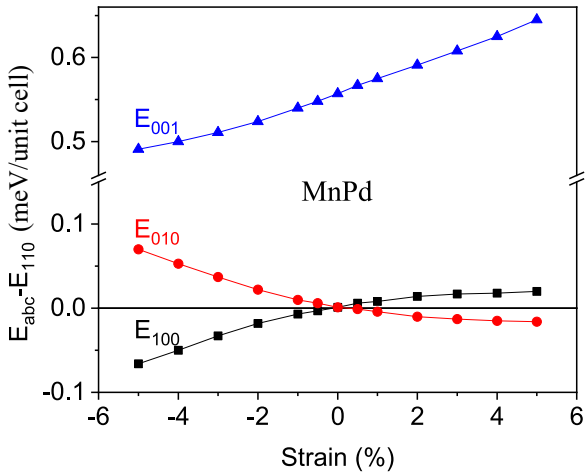

Figure 2.5: MnPd energy differences $E_{abc} - E_{110}$ for the 3 different orientations of the Néel vector as indicated by the labels.

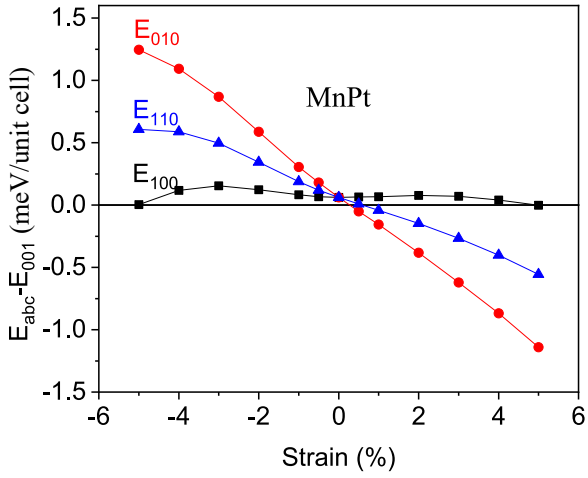

Figure 2.6: MnPt energy differences $E_{abc} - E_{001}$ for the 3 different orientations of the Néel vector as indicated by the labels.

magnets with a negative magnetostriction coefficient, since tensile strain along [100] causes the Néel vector to align in the [010] direction [34].

MnPt is unique among the 5 materials. In equilibrium, in the absence of strain, the Néel vector has perpendicular anisotropy. Under compressive (negative) strain along the [100] axis, the Néel vector remains out-of-plane. Under tensile strain along [100], the Néel vector switches from out-of-plane [001] to in-plane aligning in the [010] direction.

To understand the physical origin of 90° rotation of the Néel vector in MnPt from out-of-plane to in-plane under the tensile strain, the d-orbital resolved band structures with and without strain are plotted in Figure 2.7. Under the second order perturbation theory, the difference between two total energies with different Néel vector orientations can be approximated as [35]

$$E_{010} - E_{001} \propto \xi^2 \sum_{o,u} \frac{\left|\left\langle \Psi_o^{\downarrow} \middle| \hat{L}_z \middle| \Psi_u^{\downarrow} \right\rangle\right|^2 - \left|\left\langle \Psi_o^{\downarrow} \middle| \hat{L}_{x(y)} \middle| \Psi_u^{\downarrow} \right\rangle\right|^2}{E_u^{\downarrow} - E_o^{\downarrow}}, \tag{2.1}$$

where $\Psi_o(\Psi_u)$, $E_o(E_u)$, and ξ are the (un)occupied Bloch states, corresponding eigenvalues, and the spin-orbit coupling constant, respectively. $\hat{L}_z$ and $\hat{L}_{x(y)}$ are the out-of plane and in-plane components of the orbital angular momentum operator, and $\uparrow$ and $\downarrow$ denote spin-up and spin-down. The non-zero matrix elements in the Eq. (2.1) are $\langle d_{xz}|\hat{L}_z|d_{yz}\rangle$, $\left\langle d_{x^2-y^2}\middle|\hat{L}_z\middle|d_{xy}\right\rangle$, $\langle d_{z^2}|\hat{L}_x|d_{yz}\rangle$, $\langle d_{xy}|\hat{L}_x|d_{xz}\rangle$, $\left\langle d_{x^2-y^2}\middle|\hat{L}_x\middle|d_{yz}\right\rangle$, $\langle d_{z^2}|\hat{L}_y|d_{xz}\rangle$, $\langle d_{xy}|\hat{L}_y|d_{yz}\rangle$, and $\left\langle d_{x^2-y^2}\middle|\hat{L}_y\middle|d_{xz}\right\rangle$. The largest contributions to Eq. (2.1) come from pairs of occupied and unoccupied states at the vicinity of the Fermi level. As shown in the Figure 2.7(a), without strain, there are strong spin-orbit coupling between the occupied $d_{yz}^{\downarrow}$ and unoccupied $d_{xz}^{\downarrow}$ orbitals through $\hat{L}_z$ operator at the Z point. Since these orbitals almost touch the Fermi level, the coupling between them gives rise to the strongest contributions to the first

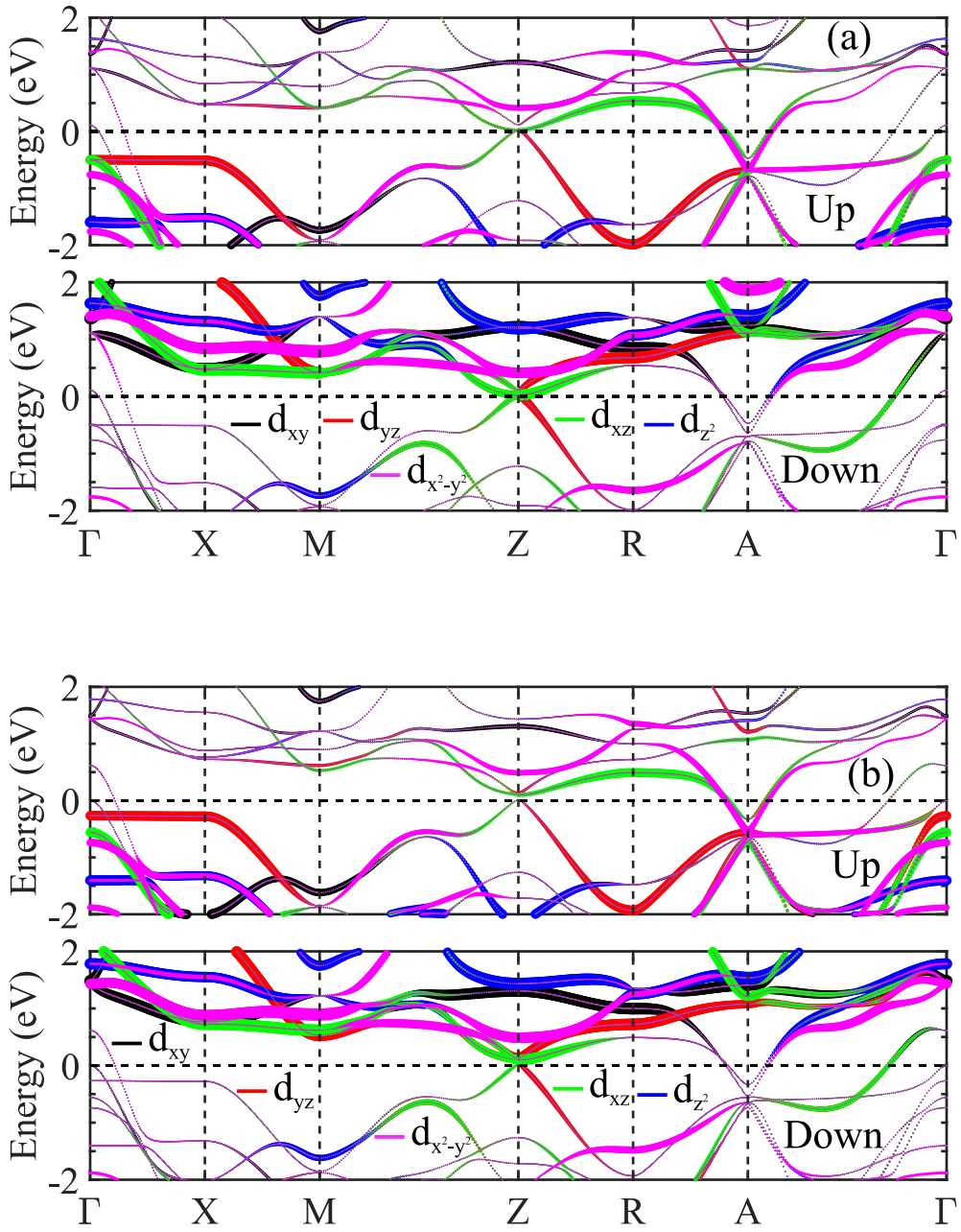

Figure 2.7: The d-orbital resolved bandstructures of MnPt (a) without strain and (b) with the applied strain of 4%. For both (a) and (b), the top and bottom panels represent up-spin and down-spin band structures, respectively. The colors indicate the different d-orbitals composition, as given by the legends. The line thicknesses indicate the relative weights.

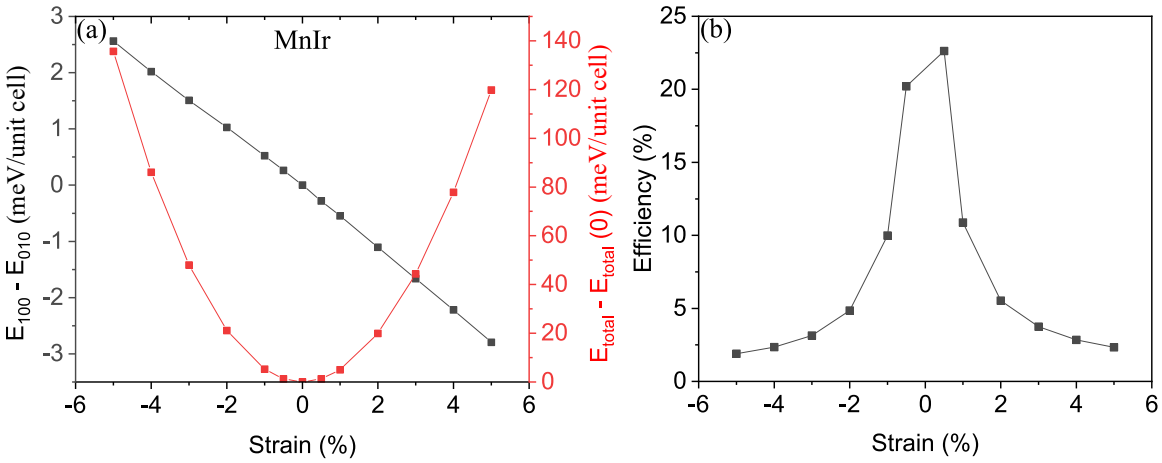

Figure 2.8: MnIr strain energies and efficiency versus strain. (a) The energy difference between two different Néel vector orientations (black) as shown by the left axis, and the change in total energy (red) as shown by the right axis. (b) The efficiency as a function of the strain.

term in the Eq. 2.1, which in this case is the perpendicular magnetic anisotropy. However, as shown in the Figure 2.7(b), the tensile strain opens a gap of 100 meV between these orbitals so that the contributions from them reduce, which results in the in-plane anisotropy.

For applications, it is useful to quantify the efficiency with which strain rotates the Néel vector and to determine the magnetostriction coefficient from the ab initio calculations. The internal efficiency is defined as

$$\text{Efficiency}(\%) = \left| \frac{E_{abc} - E_{a'b'c'}}{E_{total} - E_{total}(0)} \right| \times 100, \tag{2.2}$$

where the total energies E_{abc} and $E_{a'b'c'}$ are defined in the same way as above, i.e. the total energies in the presence of strain with the Néel vector oriented along $[abc]$ or $[a'b'c']$,

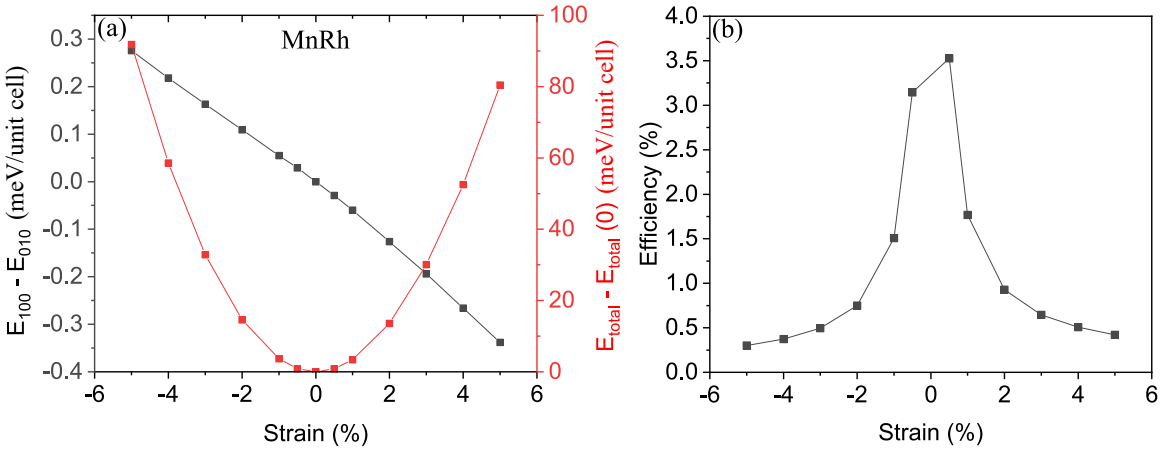

Figure 2.9: MnRh strain energies and efficiency versus strain. (a) The energy difference between two different Néel vector orientations (black) as shown by the left axis, and the change in total energy (red) as shown by the right axis. (b) The efficiency as a function of the strain.

respectively. The denominator in the Eq. (2.2) is the total energy change induced by the strain. For MnIr, MnRh, MnNi, and MnPd, E_{abc} and $E_{a'b'c'}$ are E_{100} and E_{010}, respectively. For MnPt, E_{abc} and $E_{a'b'c'}$ are E_{010} and E_{001}, respectively. The numerator and denominator of Eq. (2.2) are plotted as a function of strain in Figs. 2.8-2.12(a), and the resulting efficiencies are plotted as a function of strain in Figs. 2.8-2.12(b). The changes in the total energies, shown as red curves in Figs. 2.8-2.12(a), are parabolic so that they can be considered as the strain energy proportional to the square of the applied strain. On the other hand, the differences between two energies (the black curves in Figs. 2.8-2.12(a)) are approximately linear under small strain ($< 1\%$). Therefore, the efficiency decreases sharply as the amount of strain increases. At 0.5% strain, the highest efficiency for 90° in-plane rotation of the Néel vector is 20% for MnIr. For MnRh, MnNi, and MnPd, the efficiencies are smaller and equal to 3.5%, 1.5%, and 1.4%, respectively. To rotate the Néel vector from

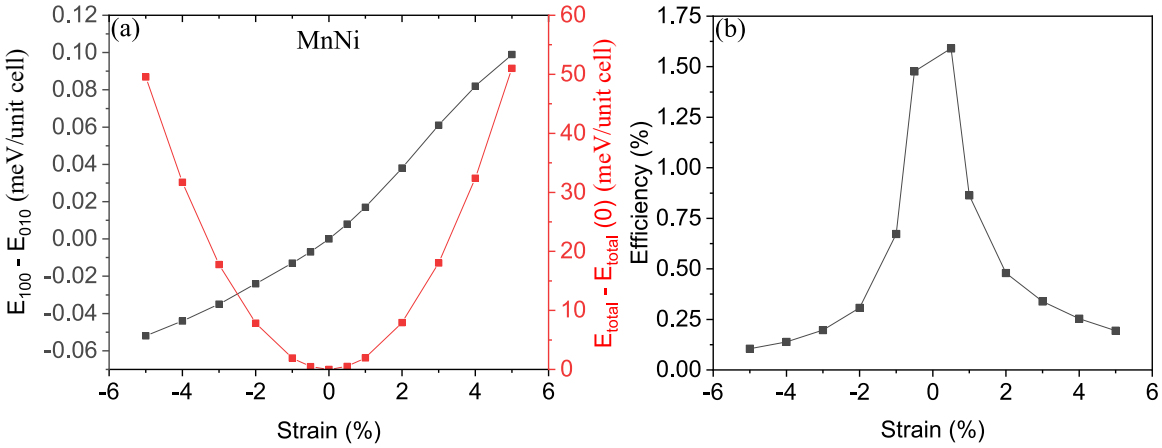

Figure 2.10: MnNi strain energies and efficiency versus strain. (a) The energy difference between two different Néel vector orientations (black) as shown by the left axis, and the change in total energy (red) as shown by the right axis. (b) The efficiency as a function of the strain.

out-of-plane to in-plane in MnPt, a positive, tensile strain must be applied. The efficiency of this process at +0.5% strain is 6%.

Using the data above, the magnetostriction coefficients (λ_s), which are widely used in ferromagnets, are calculated. The magnetostriction coefficient is defined as

$$\lambda_s(ppm) = \frac{2K_{me}}{3Y(\varepsilon_{bb} - \varepsilon_{aa})}, \tag{2.3}$$

where Y and $(\varepsilon_{bb} - \varepsilon_{aa})$ are Young's modulus and strain, respectively [36]. K_{me} is the magnetoelastic anisotropy constant, which is defined as the difference of the magnetic anisotropy energies with and without strain, and the magnetic anisotropy energy is defined as $E_{100} - E_{010}$. Plots of $E_{100} - E_{010}$ as a function of strain are shown in Appendix A Fig. A.2. Young's moduli for all MnX alloys except MnIr were adopted from previous calculation results [24, 25], and the value for MnIr was determined as described in the Appendix A. For simplicity, we disregard ε_{bb} which represents a negligible change in the lattice constant along the b-axis caused by the applied strain along a. The results for λ_s are summarized in

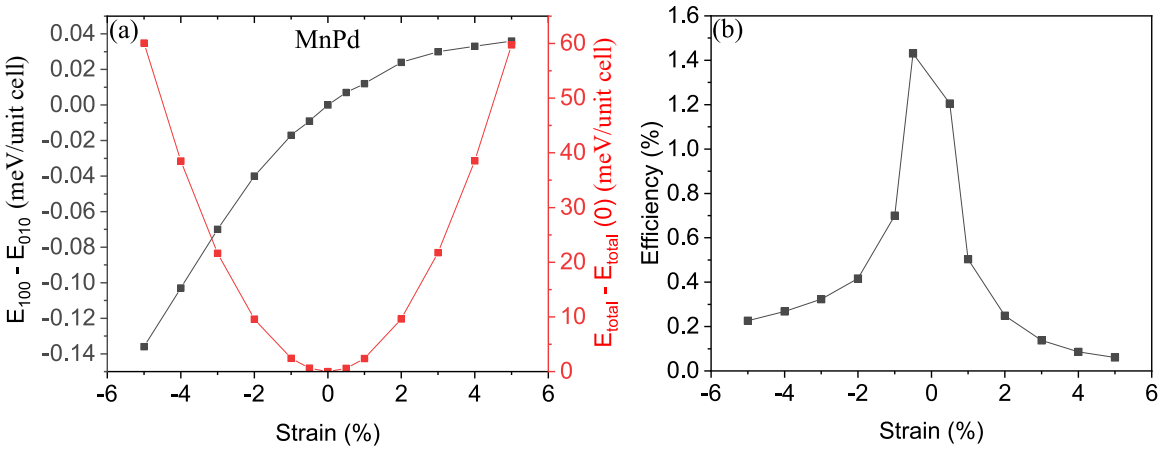

Figure 2.11: MnPd strain energies and efficiency versus strain. (a) The energy difference between two different Néel vector orientations (black) as shown by the left axis, and the change in total energy (red) as shown by the right axis. (b) The efficiency as a function of the strain.

the Table 2.2. As expected, MnIr and MnRh have positive values of λ_s, and MnNi, MnPd, and MnPt have negative values. Also, the magnitudes of the magnetostriction coefficients follow the magnitudes of the efficiencies. The magnetostriction coefficients of the MnX alloys are comparable with the ones from ferromagnets [37–41], which suggests that strain can be used to control the magnetic anisotropy of these antiferromagnetic materials.

Table 2.2: Calculated magnetrostriction coefficients of the $L1_0$-type MnX alloys.

	MnIr	MnRh	MnNi	MnPd	MnPt
λ_s (ppm)	241	43	-15	-17	-196

2.4 Summary and Conclusions

In summary, the Néel vectors of MnIr, MnRh, MnNi, and MnPd can be rotated 90° in the basal plane by applying in-plane strain. MnIr and MnRh behave like magnets

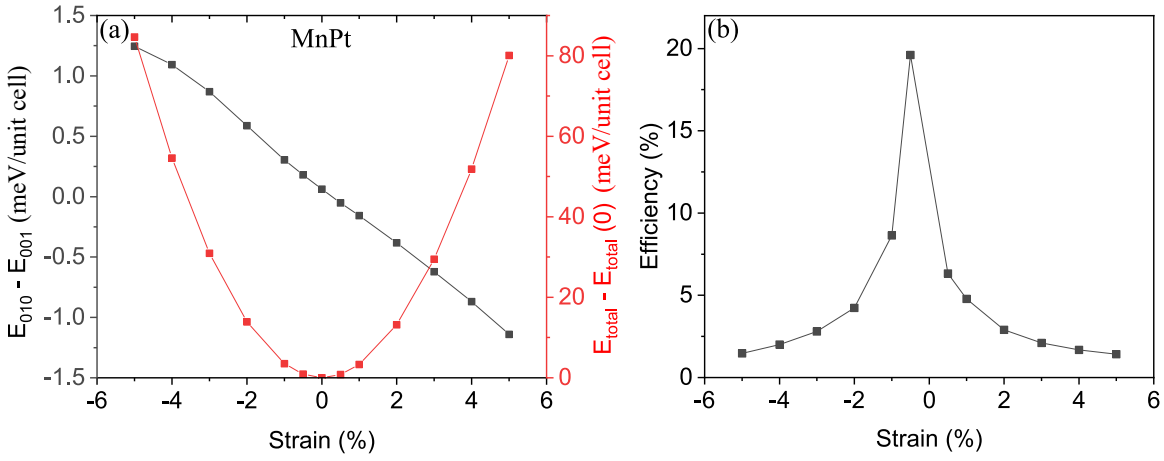

Figure 2.12: MnPt strain energies and efficiency versus strain. (a) The energy difference between two different Néel vector orientations (black) as shown by the left axis, and the change in total energy (red) as shown by the right axis. (b) The efficiency as a function of the strain.

with positive magnetostriction coefficients, since their Néel vectors align with tensile strain. MnNi and MnRh behave like magnets with negative magnetostriction coefficients, since their Néel vectors align with compressive strain. The internal efficiency of this process is highest for MnIr and it is equal to 20% at 0.5% strain. MnPt is unique among the 5 alloys in that its Néel vector aligns out-of-plane along the [001] axis in equilibrium. Applying a tensile strain along [100] rotates the Néel vector from out-of-plane [001] to in-plane [010]. The efficiency of this process at 0.5% tensile strain is 6%. Under compressive strain along [100], the Néel vector of MnPt remains out-of-plane [001]. The magnitudes of the calculated magnetostriction coefficients are comparable with those of ferromagnets, and they follow the same trends as the calculated efficiencies. For in-plane rotation of the Néel vector, MnIr has the highest magnetostriction coefficient of 241 ppm. The magnetostriction coefficient for out-of-plane rotation in MnPt is -196 ppm. These results suggest that strain can be an effective mechanism to control the Néel vectors in this family of antiferromagnets.

Chapter 3

Effects of filling, strain, and electric field on the Néel vector in antiferromagnetic CrSb

3.1 Introduction

Antiferromagnetic (AFM) materials are of great interest for future spintronics applications [17]. Their resonant frequencies are much higher than those of ferromagnetic (FM) materials, which allows them to be used in the THz applications [8–10] and ultrafast switching [12]. However, it is challenging to control and detect the antiferromagnetic states. There are several methods to control the spins in AFMs such as via exchange bias with a proximity FM layer [42] and the use of electric current by Néel spin-orbit torque [26]. The latter method has been extensively studied, although the results have recently been

questioned [43, 44]. Controlling the Néel vector without electric current is promising for ultra low power applications, since it has been predicted that magnetization reversal can be achieved with atto joule (aJ) level energy consumption [11]. Electric field control of the magnetic properties of AFMs can be realized indirectly through the mechanism of mechanical strain created from a piezoelectric substrate [1, 29, 30, 45–48] or a combination of strain plus exchange spring [49]. It can also be realized directly through the mechanism of voltage controlled magnetic anisotropy (VCMA). This mechanism has been experimentally and theoretically studied for FMs [50–71], and the experimental results have been recently reviewed. [72] Technological applications have been described and analysed [73–75]. More recently, several theoretical studies of VCMA in the AFM materials FeRh, MnPd, and MnPt have been reported [12, 76–78].

CrSb crystallizes in the hexagonal NiAs-type structure, and the spins on the Cr atoms couple ferromagnetically within the hexagonal plane and antiferromagnetically along the hexagonal axis as shown in Fig. 3.1(a). In the ground state, the Néel vector aligns along the hexagonal axis ([0001] direction), so that it has perpendicular magnetic anisotropy (PMA). The bands near the Fermi energy are composed of the d-orbitals of the Cr atoms, and these bands give rise to a large peak in the density of states near the Fermi energy. [79–82] The Sb atoms provide significant SOC. CrSb has a high Néel temperature (705 K) making it suitable for on-chip applications [16]. Recently, CrSb has been used to control the magnetic textures and tune the surface states of topological insulators [83–85].

We examine three different physical mechanisms that alter the magnetic anisotropy of bulk and thin-film CrSb: (i) strain, (ii) electron filling, and (iii) electric field. Density

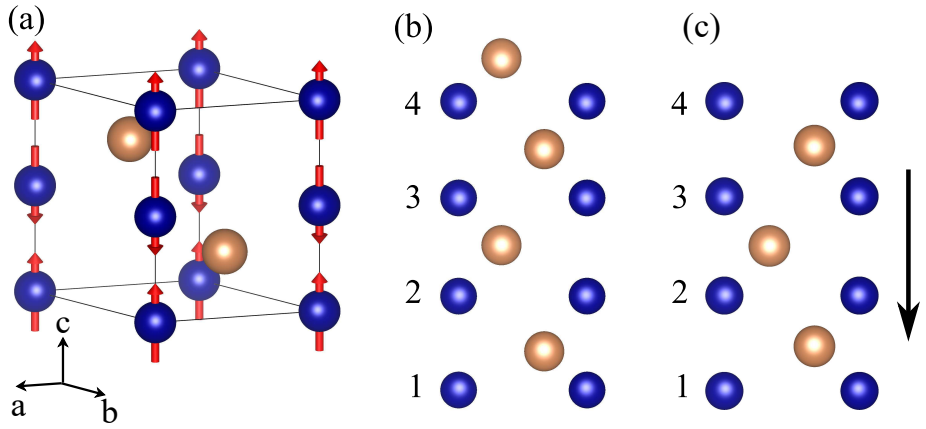

Figure 3.1: (a) Bulk antiferromagnetic CrSb crystal structure and spin texture in the ground state. Blue and brown spheres indicate the Cr and Sb atoms, respectively. (b) 1.1 nm thin film with a thickness of 2 unit cells. (c) The same thin film as in (b) but with the top Sb layer removed. The numbers index the Cr atoms, and the arrow indicates the direction of positive applied external electric field for VCMA calculations.

functional theory (DFT) calculations of the magnetostriction coefficient, strain coefficient, filling coefficient, and VCMA coefficient characterize the effectiveness of the three methods in modifying the MAE.

3.2 Methods

We perform first principles calculations as implemented in the Vienna Ab initio Simulation Package (VASP) [31] to investigate the effects of strain, electric field, and band filling on the magnetic anisotropy of CrSb. Projector augmented-wave (PAW) potentials [32] and the generalized gradient approximation (GGA) parameterized by Perdew-Burke-Ernzerhof (PBE) are employed [33]. A cut-off energy of 500 eV and $8 \times 8 \times 8$ Γ-centered k-point grid were used to make sure the total energy converged within 10^{-7} eV per unit cell. A GGA+U implementation was also used to reproduce the magnetic moment on the

Cr atom corresponding to the experimental values [86]. We used $U_{eff} = 0.25$ eV for the Cr atom where $U_{eff} = U - J$.

From the initial bulk structure, uniaxial strain along the x-axis is applied and the structure is fully relaxed along y and z axes until all forces on each atom are less than 10^{-3} eVÅ^{-1}. Here, the x and z axes are parallel to the a and c lattice vectors of the hexagonal unit cell shown in the Fig. 3.1. The strain is defined as $\varepsilon = (a - a_0)/a_0 \times 100\%$ where a and a_0 are the lattice constants along x with and without strain, respectivley. The calculated lattice constants without strain are $a_0 = 4.189$ Å and $c_0 = 5.394$ Å, which are close to those from experiment [86].

To obtain the charge density, a spin-polarized self-consistent calculation is performed with the relaxed structure for each strain. Using the obtained charge densities, $E_{\parallel}$ and $E_{\perp}$, are calculated in the presence of SOC where $E_{\parallel}$ and $E_{\perp}$ are the total energies per unit cell with the Néel vector along [1000] and [0001] directions, respectively. The magnetic anisotropy energy (MAE) is defined as $E_{\mathrm{MAE}} = E_{\parallel} - E_{\perp}$. For uniformity of comparison between bulk and thin-film structures, all values of E_{MAE} are reported per bulk unit cell (u.c.) (i.e. per two Cr atoms). For MAE calculations, a denser k-point grid ($16 \times 16 \times 16$) is used for accuracy. The same procedures are performed to investigate the effect of electron filling on the MAE, and the structures are optimized for each number of electrons in the unit cell.

Charge transfer between the Cr and Sb ions is analyzed by calculating both the Bader charges [87] and the planar averaged volumetric charge densities [88]. The "net electronic charge" on each atom is defined as the number of valence electrons for a given

atom minus the Bader charge on the atom in units of $|e|$. Thus, a depletion of electrons is a positive electronic charge. The Bader charges are used to understand the effect of truncation of the bulk to a slab and the application of an electric field. For thin-films, the planar averaged volumetric charge densities at different electric fields are calculated by averaging the three-dimensional charge density over the $x-y$ plane for fixed positions z on the c axis.

To investigate the effect of strain and electric field on the MAE of thin-film CrSb, we consider slab structures consisting of 2 and 3 unit cells along the c-axis ($\sim$ 1.1 nm and 1.6 nm). A 15 Å vacuum layer is included. The stability of two different surface terminations is quantified by calculating the cohesive energy defined as $E_{\text{coh}} = (E_{\text{crystal}} - E_{\text{isolated}})/N$ where N is the total number of atoms, E_{crystal} is the total energy of the relaxed slab structure, and E_{isolated} is the sum of the energies of the individual atoms. For the thin-film structures, a $23 \times 23 \times 1$ Γ-centered k-point grid with a 500 eV cutoff energy is used to ensure the same convergence criteria as the bulk structure. The structures are fully relaxed until all forces on each atom are less than 10^{-3} eVÅ^{-1} without changing the volume. Vertical external electric fields are applied to the slab by introducing a dipole layer in the middle of the vacuum layer. The dipole layer also corrects for the built in dipole moment in the CrSb slab structures to prevent interactions between the artificial periodic images [89, 90]. The equilibrium charge density is obtained by performing a spin-polarized self-consistent calculation without the electric field. Then, the charge densities with increasing applied electric fields along c-axis are obtained by relaxing the charges from the calculation with the previous electric field. For each electric field, the MAE is calculated using a $46 \times 46 \times 1$ k-point grid.

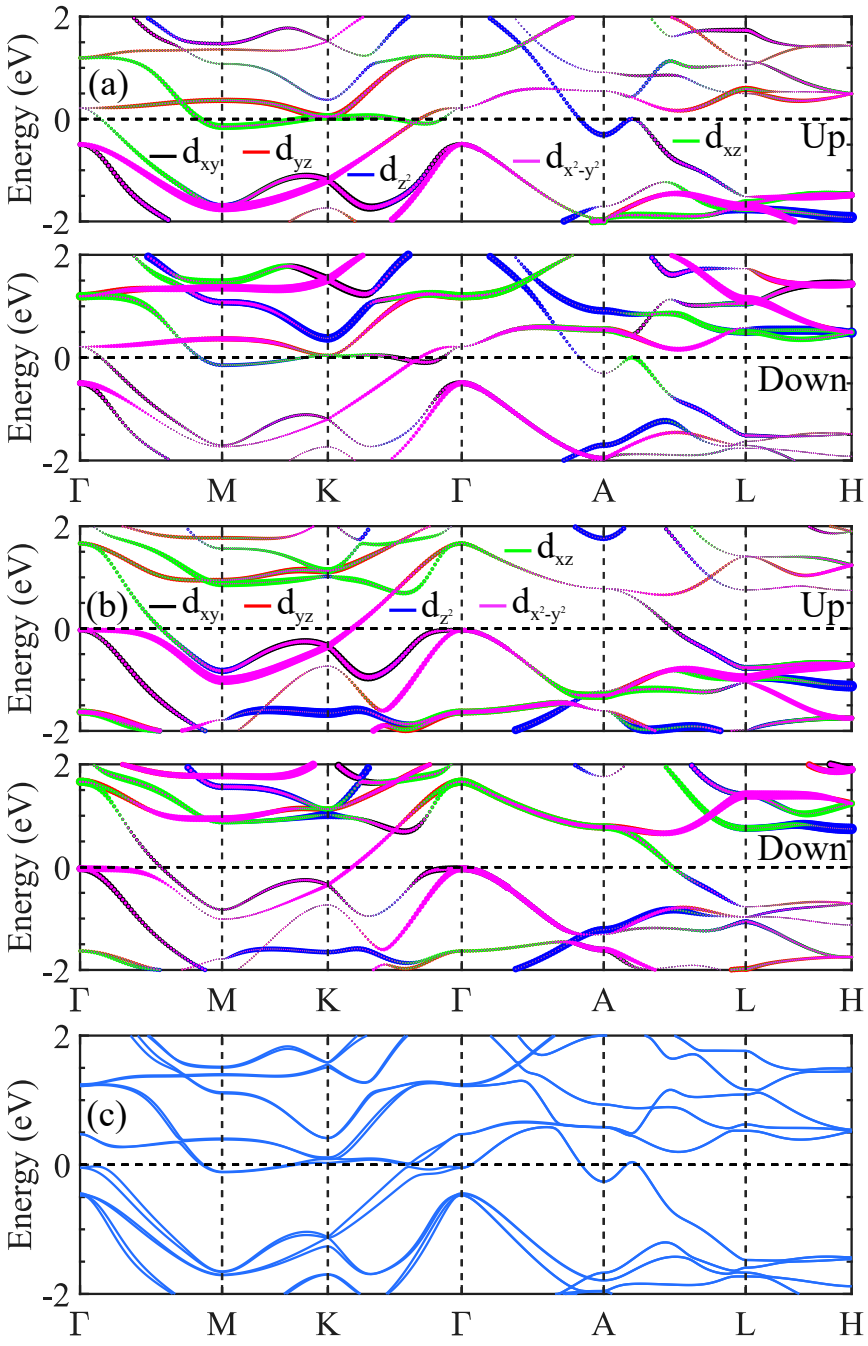

Figure 3.2: The d-orbital resolved bandstructures (without SOC) of bulk CrSb when the electron number is (a) 22 (equilibrium) and (b) 21. For both (a) and (b), the top panel is for spin up, and the bottom panel is for spin down. The colors indicate the different d-orbitals, as indicated by the legends. The line thicknesses indicate the relative weights. (c) The bandstructure of CrSb in equilibrium with SOC.

3.3 Results and Discussion

In Fig. 3.2, the electronic bandstructure of bulk CrSb is shown. Fig. 3.2(a) is the d-orbital resolved bandstructure for a Cr atom in equilibrium in the absence of SOC. The colors denote different orbitals as indicated by the legends, and the line thicknesses denote the relative occupations. The spin-up bands are shown in the top panel, and the spin-down bands are shown in the bottom panel. Fig. 3.2(c) shows the equilibrium bandstructure in the presence of SOC.

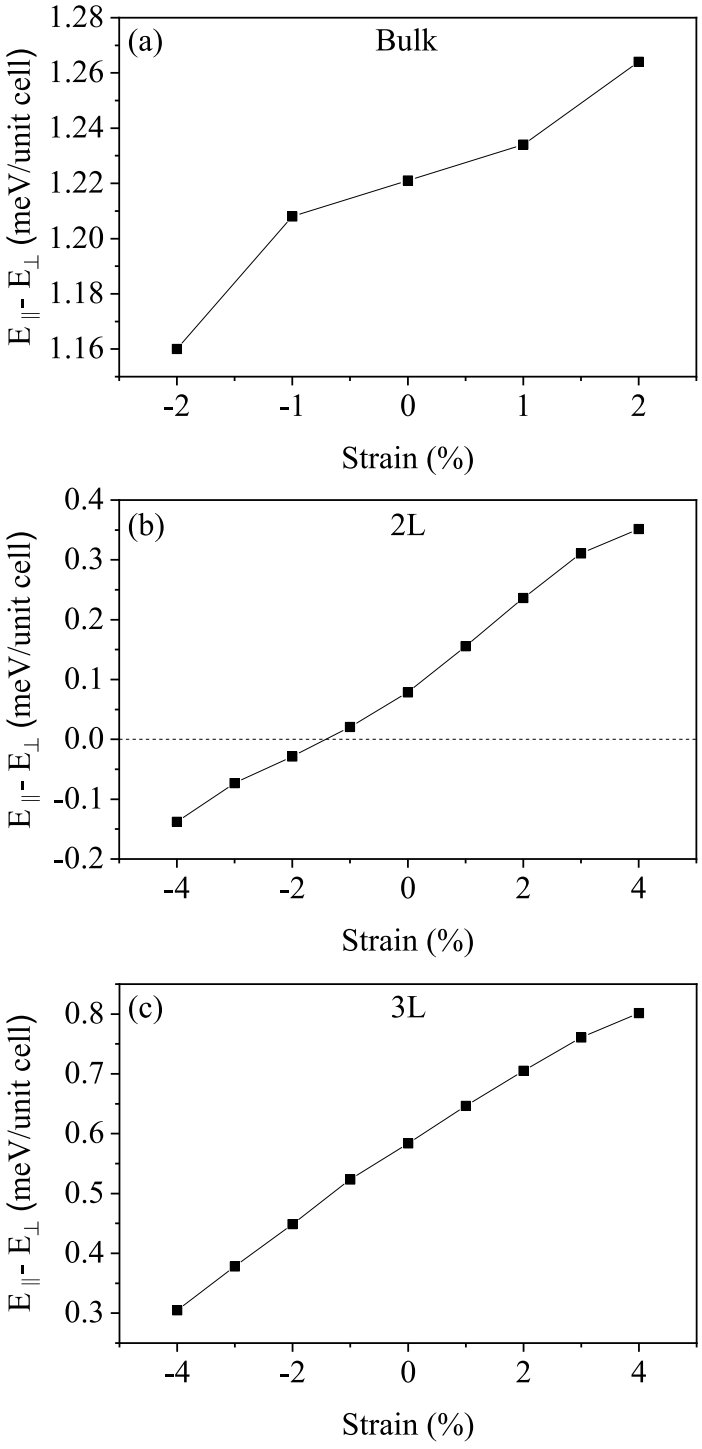

Figure 3.3: MAE as a function of applied strain for (a) the bulk crystal and for the asymmetric (b) 1.1 nm and (c) 1.6 nm thin films.

The effect of spin-orbit coupling (SOC) on the bandstructure is relatively large. A comparison of Fig. 3.2(a) to 3.2(c) shows that the SOC breaks the spin degeneracy throughout much of the Brillouin zone and creates anti-crossings at a number of band-crossing points. The largest band splitting occurs at Γ. The two bands that touch at 0.2 eV in the absence of SOC are split by ~ 0.5 eV and the hole like band is pushed down below E_F.

Fig. 3.3(a) shows E_{MAE} plotted as a function of applied strain for bulk CrSb. The value at zero strain is $E_{\mathrm{MAE}} = 1.2$ meV/u.c. The positive sign of the MAE means that the Néel vector aligns along the c-axis (out-of-plane) independent of the strain. The monotonic increase in the MAE indicates that CrSb behaves like a magnet with a negative magnetostriction coefficient, since the tensile strain favors out-of-plane anisotropy. The magnetostriction coefficient (λ_s) is defined as

$$\lambda_s(ppm) = -\frac{2K_{me}(1-v^2)}{3E\varepsilon}, \tag{3.1}$$

where v, E, and ε are the Poisson's ratio (0.288), Young's modulus (78.3 GPa), and strain, respectively [91]. The magnetoelastic anisotropy constant, K_{me}, is calculated from the difference between two MAEs with and without strain (i.e., $E_{\mathrm{MAE}}(\varepsilon) - E_{\mathrm{MAE}}(0)$). The parameters v and E are taken from a previous study [92]. The calculated λ_s for small strain (between -1 % to 1 %) is -19.8 ppm. CrSb has a negative value of λ_s, and the magnitude of λ_s is similar to that of MnNi and MnPd [1]. We also define a strain coefficient as $\alpha_\varepsilon = dE_{\mathrm{MAE}}/d\varepsilon$ evaluated at $\varepsilon = 0$. The value for bulk CrSb is $\alpha_\varepsilon = 0.013$ meV/%strain.

The response of the bulk MAE as a function of the electron number in the unit cell is shown in Fig. 3.4. In equilibrium, the unit cell has 22 valence electrons, which

is denoted by the vertical line in the figure. The MAE decreases most rapidly when the CrSb is depleted, and it changes sign when the hole doping reaches 0.75/u.c. For electron depletion, the filling coefficient, defined as $\alpha_n = dE_{\mathrm{MAE}}/dn$, is 2.92 meV, where n is the electron number per unit cell.

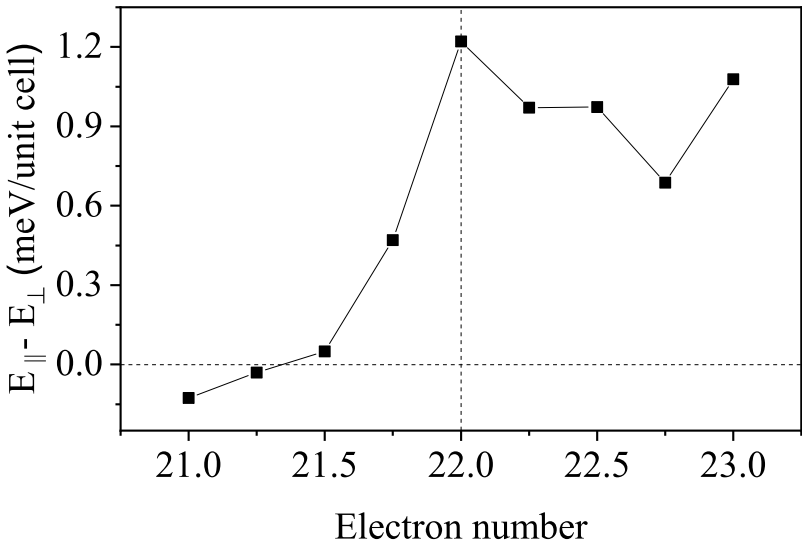

Figure 3.4: MAE of bulk crystal versus the number of electrons in the unit cell.

To understand the physical origin of the transition due to charge depletion, we consider the d-orbital resolved band structures for a Cr atom plotted for 2 different electron numbers in the unit cell, 22 (equilibrium) in Fig. 3.2(a) and 21 in Fig. 3.2(b). Within second-order perturbation theory, the MAE is approximately expressed as [35]

$$\begin{aligned} MAE \propto \xi^2 \sum_{o,u} & \frac{\left|\left\langle \Psi_o^{\uparrow}\middle|\hat{L}_z\middle|\Psi_u^{\uparrow}\right\rangle\right|^2 - \left|\left\langle \Psi_o^{\uparrow}\middle|\hat{L}_{x(y)}\middle|\Psi_u^{\uparrow}\right\rangle\right|^2}{E_u^{\uparrow} - E_o^{\uparrow}} \\ + \xi^2 \sum_{o,u} & \frac{\left|\left\langle \Psi_o^{\downarrow}\middle|\hat{L}_z\middle|\Psi_u^{\downarrow}\right\rangle\right|^2 - \left|\left\langle \Psi_o^{\downarrow}\middle|\hat{L}_{x(y)}\middle|\Psi_u^{\downarrow}\right\rangle\right|^2}{E_u^{\downarrow} - E_o^{\downarrow}} \\ + \xi^2 \sum_{o,u} & \frac{\left|\left\langle \Psi_o^{\uparrow}\middle|\hat{L}_{x(y)}\middle|\Psi_u^{\downarrow}\right\rangle\right|^2 - \left|\left\langle \Psi_o^{\uparrow}\middle|\hat{L}_z\middle|\Psi_u^{\downarrow}\right\rangle\right|^2}{E_u^{\downarrow} - E_o^{\uparrow}}, \end{aligned} \tag{3.2}$$

where $(\Psi_u)\Psi_o$, $(E_u)E_o$, and ξ are the (un)occupied states, (un)occupied eigenvalues, and the spin-orbit coupling constant, respectively. $\hat{L}_z$ and $\hat{L}_{x(y)}$ are the out-of plane and in-plane components of the orbital angular momentum operator, and $\uparrow$ and $\downarrow$ denote spin-up and spin-down. The non-zero matrix elements in the Eq. (3.2) are $\langle d_{xz}|\hat{L}_z|d_{yz}\rangle$, $\langle d_{x^2-y^2}|\hat{L}_z|d_{xy}\rangle$, $\langle d_{z^2}|\hat{L}_x|d_{yz}\rangle$, $\langle d_{xy}|\hat{L}_x|d_{xz}\rangle$, $\langle d_{x^2-y^2}|\hat{L}_x|d_{yz}\rangle$, $\langle d_{z^2}|\hat{L}_y|d_{xz}\rangle$, $\langle d_{xy}|\hat{L}_y|d_{yz}\rangle$, and $\langle d_{x^2-y^2}|\hat{L}_y|d_{xz}\rangle$. The largest contributions to Eq. (3.2) come from pairs of nearly degenerate occupied and unoccupied states near the Fermi level. In equilibrium (Fig. 3.2(a)), the main contributions to the MAE come from the spin-orbit coupling between occupied $d^{\uparrow}_{xz}$ and unoccupied $d^{\uparrow}_{yz}$ states at the K point and near the Γ point, and between occupied $d^{\downarrow}_{xy}$ and unoccupied $d^{\downarrow}_{x^2-y^2}$ states near the Γ point. All of these states couple through the $\hat{L}_z$ operator, which results in the positive MAE value (out-of-plane anisotropy). When CrSb is depleted (see Fig. 3.2(b)), the entire band structure moves upward so that the main contributor states of the perpendicular anisotropy become unoccupied. This reduces the value of the MAE, and eventually reverses the sign for $n = 21.25$.

Below, we will compare the sensitivity of the bulk crystal MAE to electron filling with the sensitivity of the thin-film MAE to applied electric field. Such a comparison requires a common metric based on a common physical quantity that governs the MAE. Assuming that the common driving mechanism is the population change of the magnetic Cr atoms [62], we determine a slightly different parameter,

$$\alpha_{\bar{n}_{\mathrm{Cr}}} = dE_{\mathrm{MAE}}/d\bar{n}_{\mathrm{Cr}}, \tag{3.3}$$

where $\bar{n}_{\mathrm{Cr}}$ is the average electron number on the Cr atoms as determined from the Bader charges. Due to the strongly ionic nature of the Cr-Sb bond, only $\sim 1/3$ of the hole doping

goes to the Cr sublattice. The equilibrium charge resulting from a transfer of ~ 0.7 electrons from the Cr atom to the Sb atom is shown in Fig. 3.5(a), and the change in charge at a filling of -0.5 electrons / u.c. is shown in Fig. 3.5(b). The filling of -0.5 electrons / u.c. corresponds to -0.07 electrons / Cr atom. Using the values from Fig. 3.5(b), for hole doping, $\alpha_{\bar{n}_{\mathrm{Cr}}} = 16.2$ meV.

We now consider thin-film slabs with thicknesses of 2 and 3 unit cells corresponding to 1.1 nm and 1.6 nm, respectively. For the thinner slab, the cohesive energies are calculated for a 7 atomic layer structure of alternating Cr and Sb layers terminated on both ends with a Cr layer and for a 8 atomic layer structure (2 unit cells) terminated on one end with Cr and on the other with Sb. The cohesive energies of the 7 and 8 atomic layer structures are -3.328 eV and -3.517 eV, respectively. For the thicker slab, cohesive energies are calculated for an 11 atomic layer structure and a 12 atomic layer structure, and the cohesive energies are -3.522 eV and -3.636 eV, respectively. Thus, the slab strucures with an integer number of unit cells such that one face is a Cr layer and the opposing face is an Sb layer are the most stable, and they are the ones that we will consider first. We will refer to these structures as asymmetric slabs.

In these asymmetric slabs, inversion symmetry is broken, since one end is terminated with a Cr layer and the other end is terminated with a Sb layer. Thus, these thin films are also Janus structures. The two unit cell asymmetric thin-film is shown in Fig. 3.1(b). Below, results for strain and VCMA coefficients are presented for both the 2 and 3 unit cell asymmetric thin-films, and the in-depth microscopic analysis of the charge, magnetic moments, and electronic structure focuses on the 2 unit cell asymmetric thin-film.

In the asymmetric thin films, there is a net polarization of electron charge between the positively charged Cr layer on the bottom and the negatively charged Sb layer on the top. The excess charges on each atom, as determined from the Bader charges, in the bulk and in the 2 unit-cell slab are shown in Fig. 3.5(a,c), and it is clear that, in the slab, the charge transfer is no longer balanced layer-by-layer. The net charge polarization gives rise to a built-in electric field that alternates positively and negatively within the slab, but, its average value points from the positive Cr layer on the bottom to the negative Sb layer on the top. This built-in electric field results in a built-in potential across the slab of 1.7 eV as shown by the plot of the equilibrium planar averaged Hartree potential in Fig. 3.5(d).

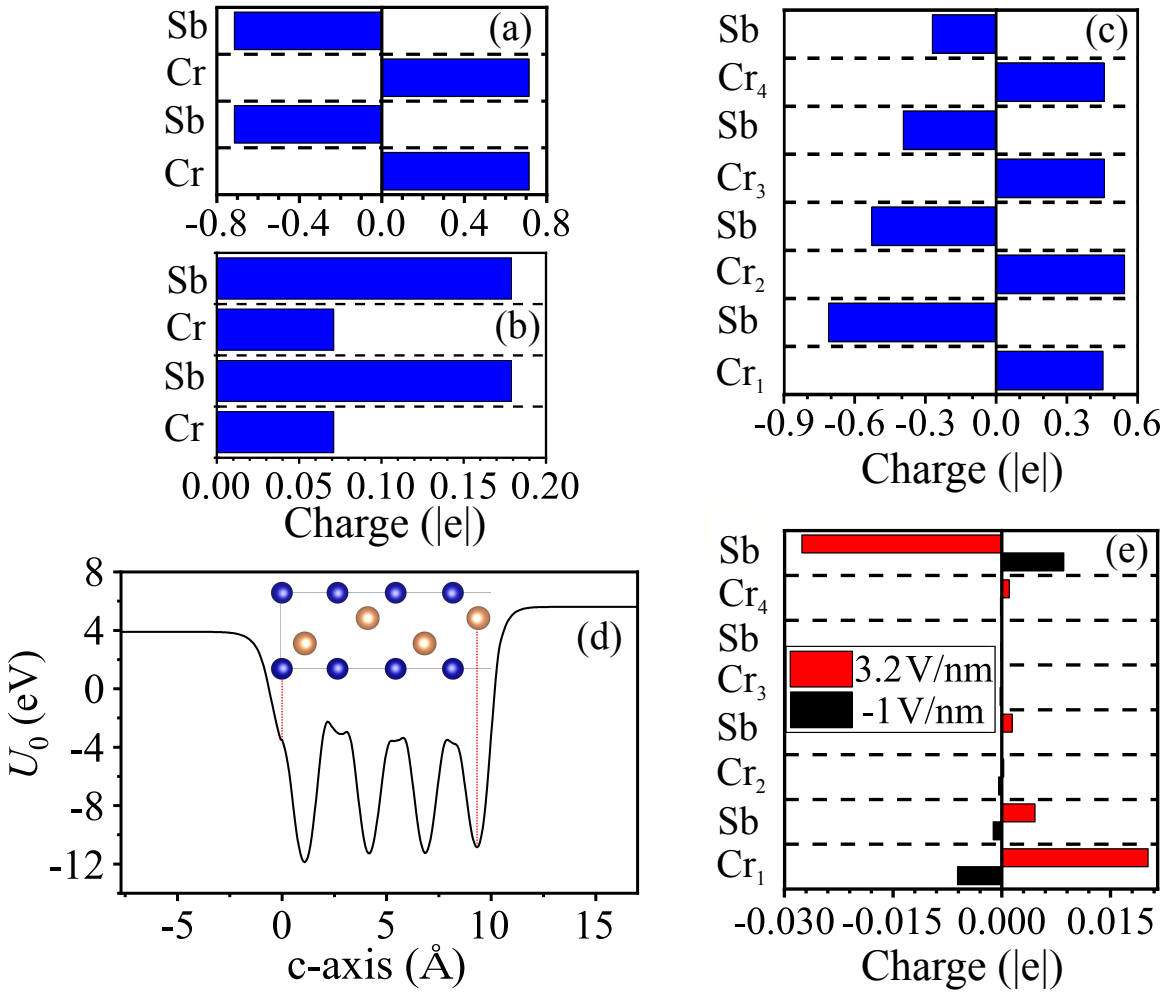

Figure 3.5: The net electronic charges on the Cr and Sb atoms, calculated from the Bader charges, in units of $|e|$, of (a) bulk and (c) 1.1 nm thin film CrSb in equilibrium. (b) Change in net electronic bulk charge due to hole doping of 0.5 holes / unit cell. (d) The planar-averaged Hartree potential of the 1.1 nm thin film CrSb in equilibrium. (e) Change in the net electronic charges induced by the electric field (indicated in the legend) with the reference charge taken from equilibrium charges shown in (c). Note that a net positive electronic charge corresponds to a depletion of the electron density.

The truncation of the bulk to a finite slab results not only in a loss of *local* balance between the positive and negative charges, but also in a *global* imbalance of the magnetic moments of the Cr ions. In other words, the cancellation of magnetic moments between alternating layers of Cr is no longer exact, and a small net magnetic moment exists in the

slab. The magnetic moments on each Cr atom are listed in the '$\mu_{\mathrm{Cr,Sb}}$' column of Table 3.1 with the numbering of the Cr atoms corresponding to that shown in Fig. 3.1(b). The magnitudes of the magnetic moments in the Cr layers monotonically decrease from bottom to top as the Cr atoms approach the Sb terminated end of the slab. The breaking of the spin degeneracy is readily apparent in the bandstructure of the slab shown in Fig. 3.6(a). The degeneracy between the up-spin and down-spin bands is broken, and the CrSb slab has become a ferrimagnet (FiM). The breaking of the spin degeneracy of the AFM states in a finite slab of a layered AFM is explained by a simple chain model with different end terminations described in [93]. The wavefunctions of a pair of degenerate AFM states are weighted differently on alternate atoms of the magnetic lattice. Thus, the coupling of the two states to an end atom is different, and this different coupling breaks the degeneracy of the two states.

Table 3.1: Magnetic moment, in units of μ_B, for each Cr atom in the bulk and thin films of Fig. 3.1 with spin-orbit coupling. The indices on the Cr atoms correspond to those in Fig. 3.1. $\mu_{\mathrm{Cr,Sb}}$ corresponds to the thin film of Fig. 3.1(b) with an integer number of unit cells, and $\mu_{\mathrm{Cr,Cr}}$ corresponds to the thin film of Fig. 3.1(c) in which the top Sb layer is removed.

Atom	μ_{bulk}	$\mu_{\mathrm{Cr,Sb}}$	$\mu_{Cr,Cr}$
Cr_1	3.035	3.763	3.905
Cr_2	−3.035	−3.190	−2.994
Cr_3		3.116	2.994
Cr_4		−2.889	−3.904

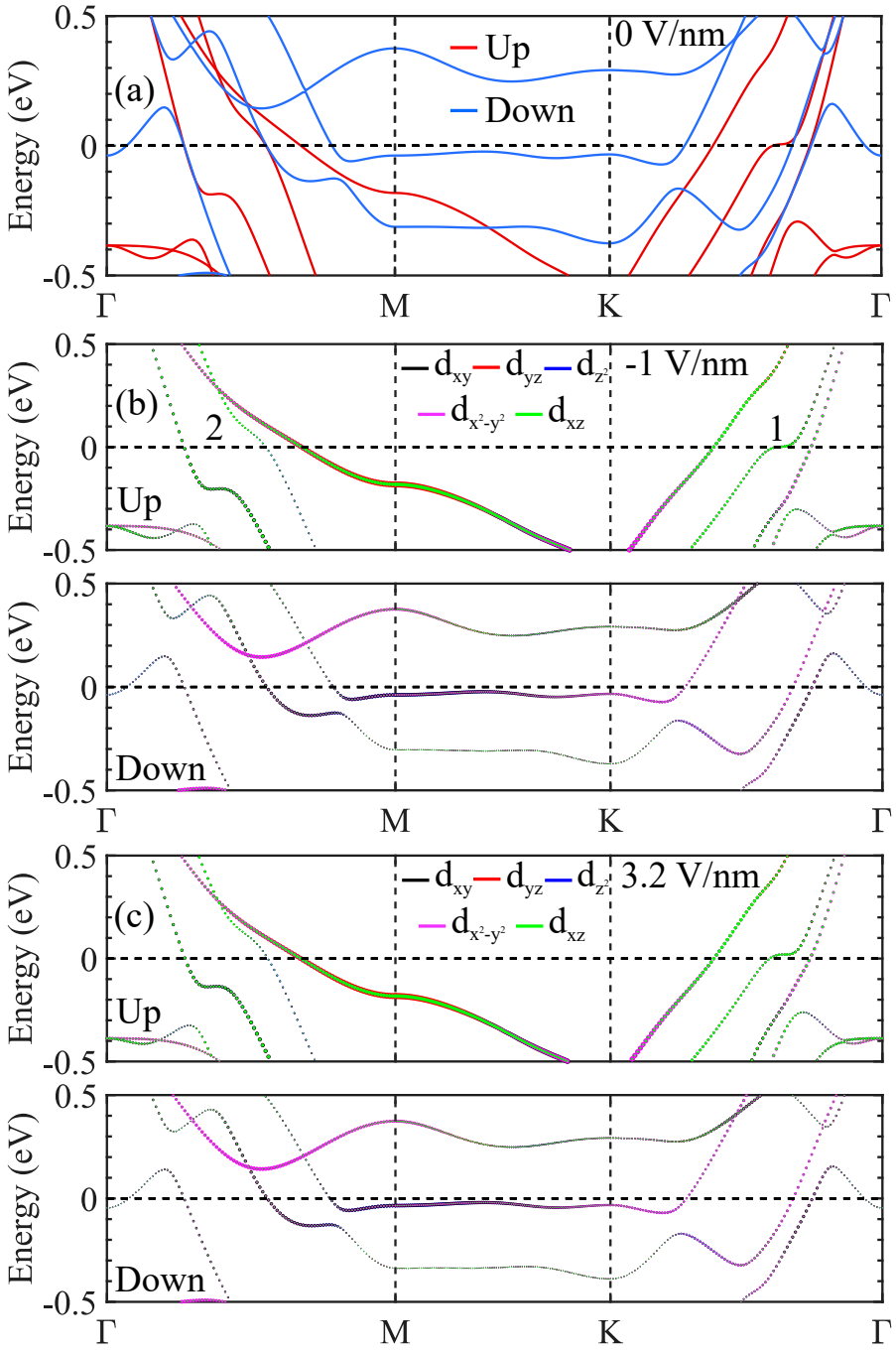

Figure 3.6: (a) Spin resolved bandstrucure of the 1.1 nm CrSb thin-film in equilibrium. (b,c) The d-orbital resolved bandstructures of the 1.1 nm CrSb thin-film under electric fields of (b) -1 V/nm and (c) 3.2 V/nm. The line colors indicate the d-orbital composition as given by the legends, and the line thicknesses indicate the relative weights.

A third result of truncating the bulk to a slab is that the MAE decreases. For the 1.1 nm slab, the MAE is reduced by a factor of 15 from 1.2 meV/u.c. to 0.079 meV/u.c. (0.17 erg/cm^2), and for the 1.6 nm slab, the MAE is reduced by a factor of 2.1 to 0.58 meV/u.c. (1.85 erg/cm^2). Also, the sensitivity of the MAE to strain increases. The strain coefficients of the 1.1 and 1.6 nm slabs (α_ε) increase from 0.013 meV/%strain in the bulk to 0.068 meV/%strain and 0.062 meV/%strain, respectively, where the energies are per bulk unit cell (2 Cr atoms). The combined result of the reduced MAE and increased strain coefficient is that a 1.5% uniaxial compressive strain along [1000] direction in the 1.1 nm thin film causes a 90° rotation of the Néel vector from out-of-plane to in-plane as shown in Fig. 3.3(b).

A fourth result is that the MAE also becomes sensitive to an external electric field as shown in Fig. 3.7. In other words, the thin slab exhibits intrinsic VCMA. Typically VCMA is found when a magnetic layer is placed in contact with a heavy-metal layer that provides SOC. However, the Sb layers provide large SOC, and the terminating Sb layer serves as the HM layer, such that the CrSb slab has intrinsic VCMA. The MAE decreases linearly as the electric field is increased, and, for the 1.1 nm slab, it changes sign at 3.2 V/nm, which indicates that the Néel vector rotates 90° from out-of-plane to in-plane.

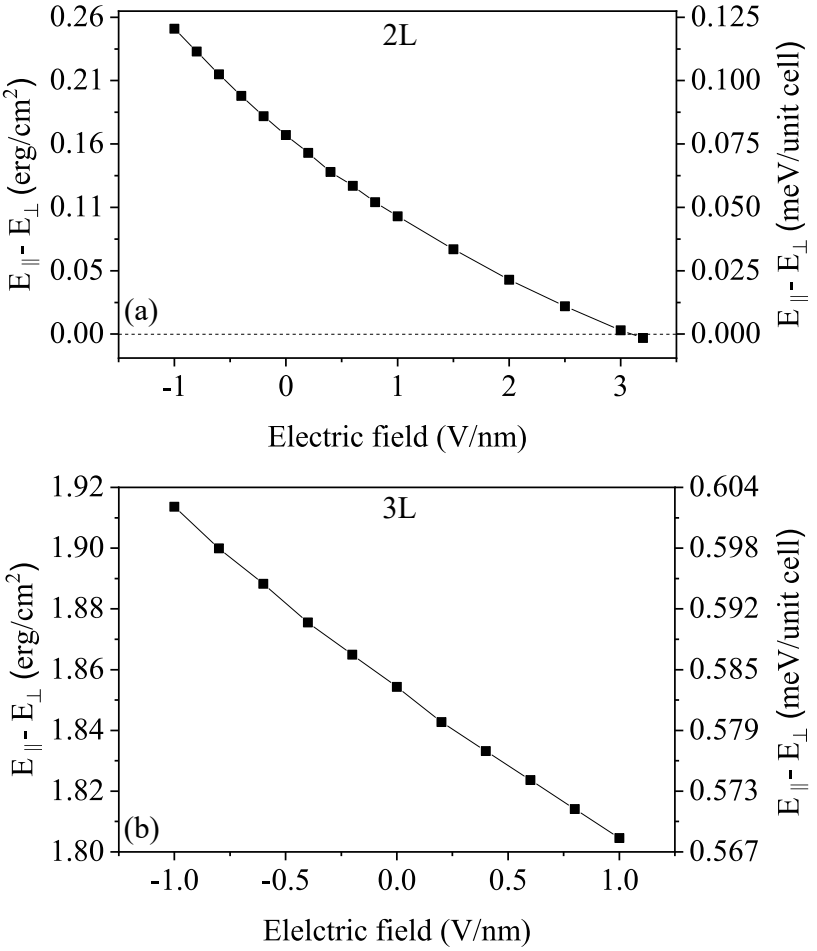

Figure 3.7: MAEs of (a) 1.1 nm and (b) 1.6 nm films as a function of applied electric field.

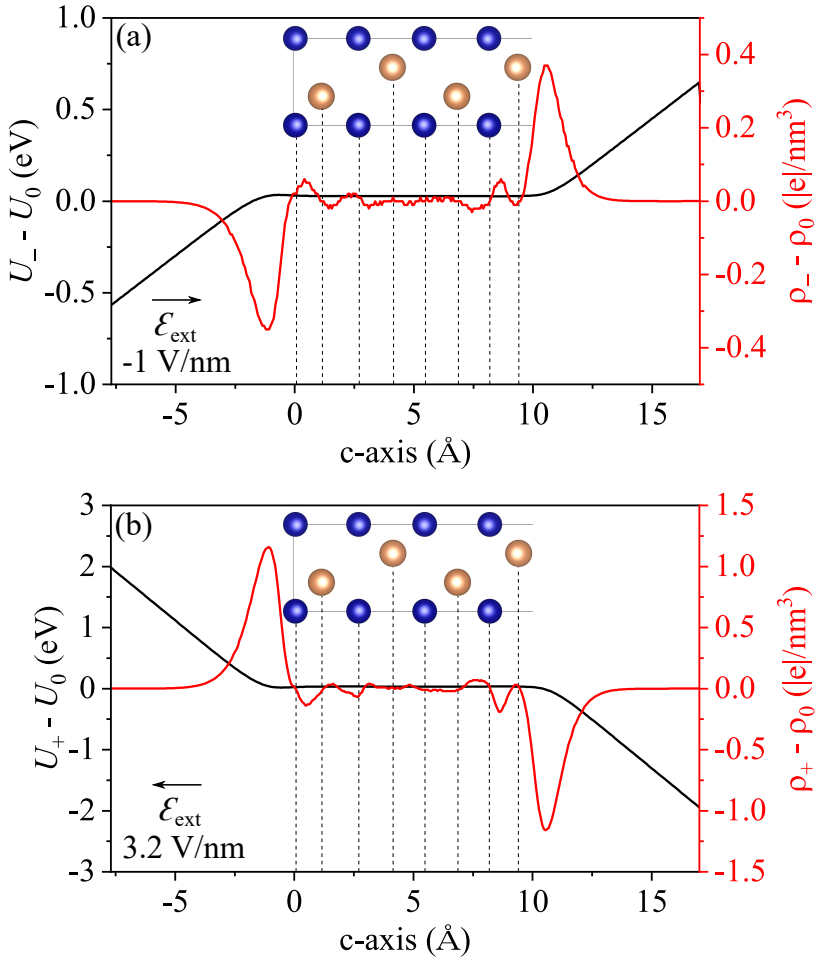

Figure 3.8: The change in the planar-averaged electronic charge (red) and planar-averaged Hartree energy (black) of 1.1 nm thin film CrSb with an electric field of (a) -1 V/nm and (b) 3.2 V/nm. The arrow indicates the direction of applied electric field. Note that a positive electronic charge corresponds to a depletion of the electron density.

The standard metric describing the sensitivity of the MAE to the applied electric field is given by the VCMA coefficient defined as

$$\beta = \frac{dE^s_{\mathrm{MAE}}}{d\mathcal{E}_I} = \frac{dE^s_{\mathrm{MAE}}}{d\mathcal{E}_{\mathrm{ext}}/\epsilon_I}, \tag{3.4}$$

where E^s_{MAE} is the MAE per unit area of the slab, $\mathcal{E}_{\mathrm{ext}}$ is the external electric field and $\mathcal{E}_I$ and ϵ_I are the electric field and the relative dielectric constant in the insulator, repectively.

In a typical experiment, the insulator would be an oxide layer with $\epsilon_I > 1$. In our case, the insulator is the vacuum, so that $\epsilon_I = 1$ and $\mathcal{E}_I = \mathcal{E}_{\text{ext}}$. The values of β, evaluated at $\mathcal{E}_{\text{ext}} = 0$ V/nm, are -76.4 fJV^{-1}m^{-1} for the 1.1 nm film and -55.3 fJV^{-1}m^{-1} for the 1.6 nm slab.

The calculated magnitudes of β are comparable with many of the experimentally measured values of β from heavy metal/FM/MgO heterostructures, [55,57–59,61,63,65,66] with magnitudes ranging from 65 fJV^{-1}m^{-1} in a Ta/$Co_{0.25}Fe_{0.55}B_{0.20}$/MgO structure [61] to 139 fJV^{-1}m^{-1} in a Ru/Co_2FeAl/MgO structure. [63] However, they are considerably smaller than the values of 370 fJV^{-1}m^{-1} and 1043 fJV^{-1}m^{-1} measured in Cr/Fe/MgO and Ir/CoFeB/MgO structures, respectively. [64,67] A lengthy table of experimental values compiled from the literature is provided in a recent review [72]. Theoretical studies of AFM materials have calculated magnitudes of β both larger and smaller than the values for CrSb. For a G-AFM FeRh/MgO bilayer, the magnitude of β was in the range of 130 to 360 fJV^{-1}m^{-1} depending on the sign of the electric field, the strain, and the termination layer of either Fe or Rh [76]. A value of 22.6 fJV^{-1}m^{-1} was calculated for Pt/MnPd with vacuum as the dielectric [77]. VCMA calculations of a MgO/MnPt/MgO slab found magnitudes of 170 fJV^{-1}m^{-1} and 70 fJV^{-1}m^{-1} depending on whether the MnPt layer was terminated on both ends with either Mn or Pt, respectively [78].

To understand which Cr atoms contribute to the VCMA effect, we inspect the change in charge of the Cr atoms in response to the applied field. The change in charge with applied electric field, plotted in Figs. 3.5(e) and 3.8, shows that, among the Cr atoms, the only significant change in charge occurs on Cr_1. This is to be expected, since the electric

field is screened by the first and last atomic layers from the interior of the CrSb metal. The first atomic layer is Cr and the last is Sb, so that an applied field creates a net change in charge on the Cr sublattice with the charge being transferred to the Sb sublattice.

The sensitivities of the MAE of the thin film slabs to the average charging of the Cr atoms due to an applied electric field is comparable to the sensitivity of the bulk MAE to the filling of the Cr atoms. The values of $\alpha_{\bar{n}_{\mathrm{Cr}}}$ evaluated at $\mathcal{E}_{\mathrm{ext}} = 0$ are 19.7 meV and 13.9 meV for the 2 layer and 3 layer slabs, respectively. For comparison, the bulk value for hole doping is $\alpha_{\bar{n}_{\mathrm{Cr}}} = 16.2$ meV. Thus, the sensitivity of the MAE per unit cell to the change in the average charge on the Cr atoms lies in the range of 13 - 20 meV for both of the slabs and the bulk.

To elucidate the physical origin of switching mechanism in the two layer slab, the d-orbital resolved band structures for the Cr_1 atom under different electric fields are plotted in Fig. 3.6(b,c). At the electric field of -1 V/nm, the major contribution of the perpendicular anisotropy comes from the spin-orbit coupling between the unoccupied $d^{\uparrow}_{xz}$ and occupied $d^{\downarrow}_{x^2-y^2}$ states through $\hat{L}_y$ operator in the region 1. Although the states in the region 1 are coupled through the in-plane angular momentum operator, the contribution of the MAE is positive since they are from different spin channels. In the region 2, the occupied $d^{\uparrow}_{xy}$ states are coupled with unoccupied $d^{\uparrow}_{xz}$ states through $\hat{L}_x$, which contributes the in-plane anisotropy. As the external field increases (see Fig. 3.6 (c)), the unoccupied $d^{\uparrow}_{xz}$ states in the region 1 move away from the Fermi level by 18 meV, which results in the reduction of the out-of-plane anisotropy, since the denominator in the Eq. 3.2 increases. In

addition, in the region 2, the occupied $d_{xy}^{\uparrow}$ states move closer to the Fermi energy by 67 meV as the electric field increases so that the in-plane anisotropy increases.

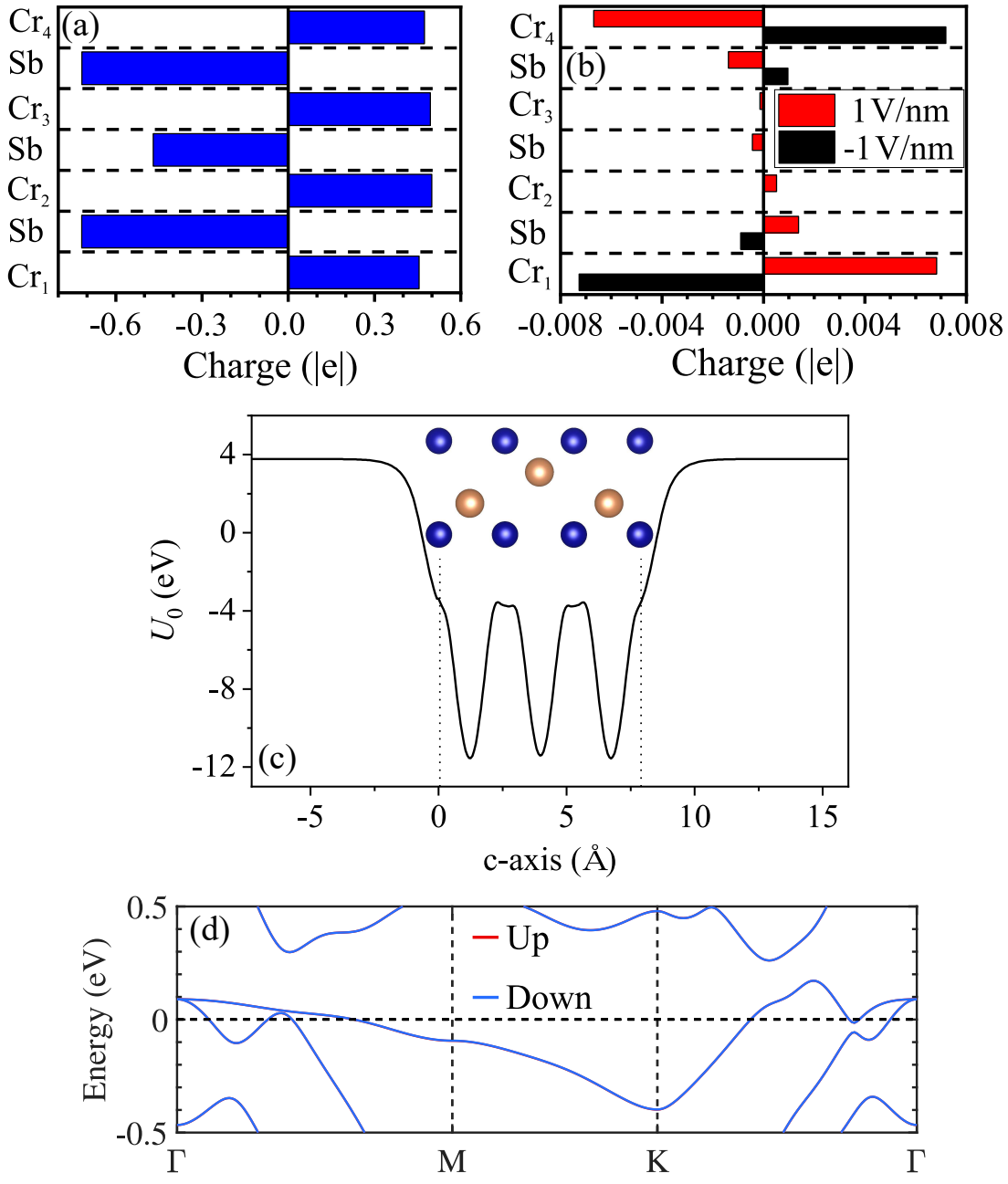

Figure 3.9: The net electronic changes on the Cr and Sb atoms from Bader charge calculations in the units of $|e|$ in the symmetric thin film. (b) Change in the net electronic charges induced by different electric fields (indicated in the legend) with the reference charge taken from equilibrium charges shown in (a). (c) The planar-averaged Hartree potential of the symmetric thin film CrSb in equilibrium. (d) The spin-resolved bandstructure of the symmetric thin film CrSb in equilibrium.

Previous studies have shown that the choice of surface termination of a FM layer can alter, or even change the sign of the MAE [76,78,94,95]. Thin film CrSb is no exception. The final structure that we consider is the slab shown in Fig. 3.1(c). It is identical to the 1.1 nm thin film analyzed above, except that the top Sb layer is removed so that the thin film becomes mirror symmetric with respect to the $x - y$ plane. As a result, there is no net electrical dipole moment or built-in potential across the slab (see Fig. 3.9(a) and (c)). The net magnetic moment of the slab remains zero, as shown in the last column of Table 3.1. The zero net magnetic moment manifests that the slab is antiferromagnet, which is confirmed by the doubly degenerated bandstructure, as shown in Fig. 3.9(d). The magnetic moment is no longer compensated locally in each unit cell; the compensation occurs between the mirror symmetric pairs of Cr atoms. Furthermore, the magnitude of the MAE (-1.07 meV / u.c) is more than an order of magnitude larger compared to that of the asymmetric slab (0.079 meV / u.c), and it changes sign, so that in-plane alignment of the magnetic moments is preferred. The magnitude of the MAE is similar to that of the bulk (1.2 meV / u.c), but with opposite sign. Note that the value of -1.07 meV / u.c. is obtained by taking the total MAE of the slab and dividing by two, since it contains two unit cells of magnetic ions even though the last Sb layer of the top unit cell is missing.

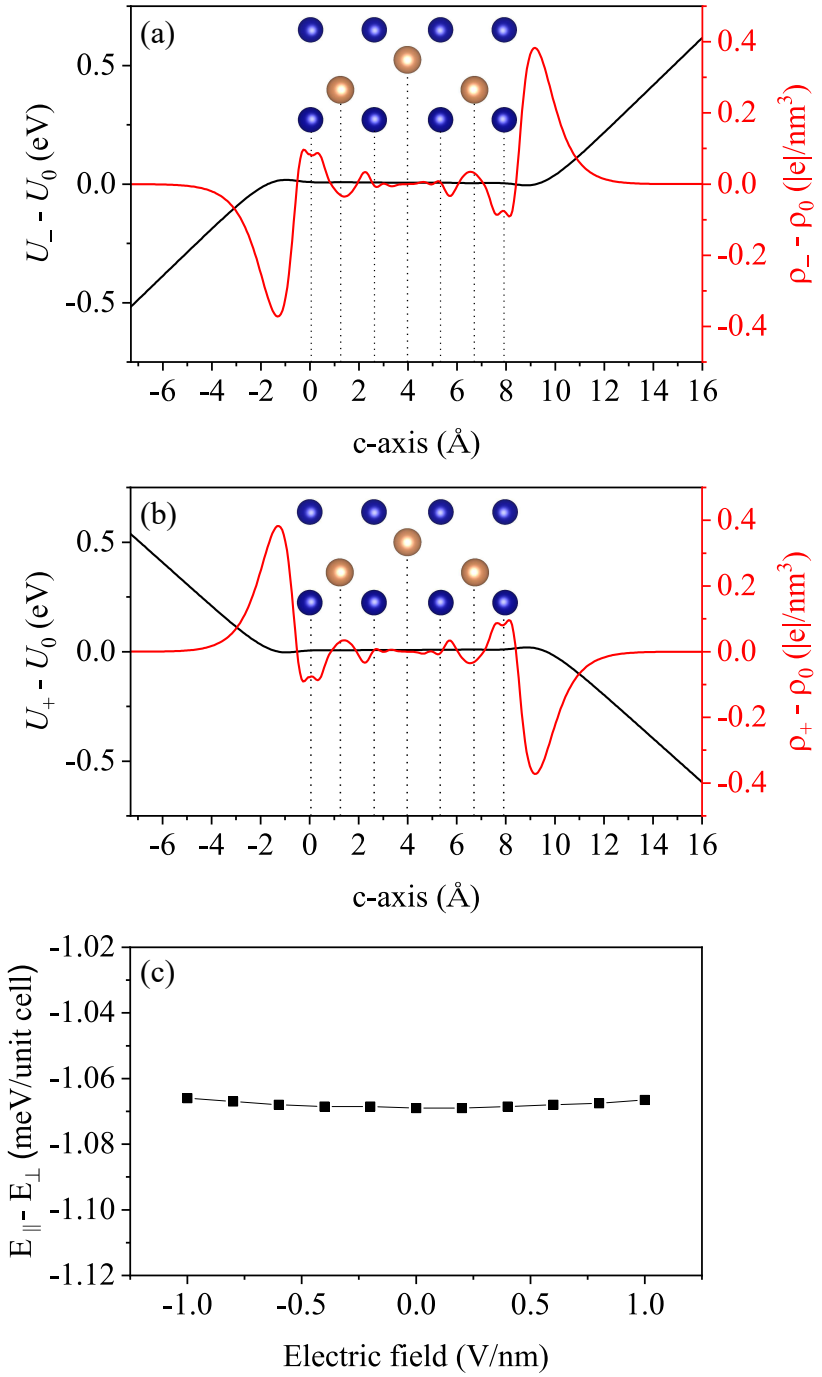

Figure 3.10: The change in the planar-averaged electronic charge (red) and Hartree potential (black) of the symmetric thin film CrSb at the electric field of (a) -1 V/nm and (b) 1 V/nm. (c) MAE as a function of electric field.

Applying an electric field to this symmetric slab depletes electrons from the bottom Cr layer and accumulates electrons on the top Cr layer, so that the net change in charge on the Cr layers is zero as shown in Figs. 3.9(b) and 3.10 (a) and (b). This is in contrast to the effect of an electric field on the antisymmetric slab where the applied field depletes electrons from the bottom Cr layer and accumulates electrons on the top Sb layer, with the overall effect being a net depletion of electrons on the Cr atoms. In the symmetric slab, with no net change in charge on the Cr atoms, the MAE remains unchanged to 4 significant digits over the range of $-1 \leq \mathcal{E}_{\text{ext}} \leq 1$ V/nm (see Fig. 3.10 (c)). This is consistent with results of prior simulations of symmetric MgO / FM / MgO and MgO / AFM / MgO structures [50, 78].

To estimate the sensitivity of the MAE of the symmetric slab to electron filling, we alter the electron number of the slab by applying a compensating background charge, as we did in the bulk. Since the background charge is uniformly distributed throughout the simulation domain, which includes the vacuum region, the majority of the compensating charge in the CrSb slab is located on the outer two Cr layers. Depleting 0.5 electrons from the CrSb slab results in a total reduction of 0.32 electrons from the Cr sublattice with an average reduction of 0.080 electrons from the Cr atoms. The MAE changes from -1.07 meV to -0.7 meV, so that $\alpha_{\bar{n}_{\text{Cr}}} = -4.6$ meV. The negative sign means that as electrons are removed, the in-plane orientation of the Néel vector becomes less stable. The magnitude of $\alpha_{\bar{n}_{\text{Cr}}}$ is a factor of 4 less than that of the asymmetric slab, and the sign is opposite. Thus, the mirror symmetric slab of just 4 Cr layers has a high in-plane MAE, similar in magnitude to that of the bulk, and it is relatively insensitive to filling. Physically realizing such a structure would be challenging.

In a typical physical structure, the CrSb slab will be sandwiched between a MgO layer on one face and a grounded heavy-metal (HM) layer on the opposing face. The electric field in the dielectric MgO will terminate at the CrSb where it will accumulate or deplete charge on the first atomic layer of the CrSb as shown at the left of Fig. 3.8. In the physical structure, there is no corresponding charge depletion or accumulation on the opposing face of the CrSb slab, since the HM is grounded and supplies the charge required to screen the electric field at the MgO/CrSb interface. Also, there will naturally be asymmetry and a built in potential across the CrSb slab due to the proximity of MgO on one face and a HM on the other. Since breaking the mirror symmetry of the slab breaks the degeneracy of the AFM states, it is most probable that the CrSb in a MgO/CrSb/HM structure will be in a FiM state. For the electric field in the MgO to significantly alter the charge on the Cr sublattice, the CrSb should be terminated with a Cr layer at the MgO interface.

Finally, we note that the parameter $\alpha_{\bar{n}_{\mathrm{Cr}}}$, which gives the sensitivity of the MAE to the magnetic sublattice filling, is simply related to the conventional VCMA parameter β by

$$\alpha_{\bar{n}_{\mathrm{Cr}}} \approx -\frac{2|e|}{\epsilon}\beta, \tag{3.5}$$

where $\epsilon = \epsilon_0\epsilon_I$, is the dielectric constant of the insulator, and the the negative sign is consistent with the sign of the positive electric field and the orientation of the slab in Fig. 3.1. The sign would reverse if either the field or the slab were reversed. Equation (3.5) is derived by noting that the induced charge lies primarily on Cr_1, and, therefore, it can be approximated as a sheet density of an ideal metal given by $n_s = n_{\mathrm{Cr}_1}/A_{u.c.} \approx \bar{n}_{\mathrm{Cr}} N_L^{\mathrm{Cr}}/A_{u.c.} \approx -\epsilon\mathcal{E}$ where $A_{u.c.}$ is the area of the unit cell in the basal plane, and N_L^{Cr} is

the number of Cr layers in the slab. Also, $E^s_{\mathrm{MAE}} = E_{\mathrm{MAE}} N_{u.c.}/A_{u.c.}$ where $N_{u.c.} = N_L^{\mathrm{Cr}}/2$. With these relations, we can write, $dE_{\mathrm{MAE}}/d\bar{n}_{\mathrm{Cr}} \approx -\frac{2|e|}{\epsilon} dE^s_{\mathrm{MAE}}/d\mathcal{E}$, which is Eq. (3.5). This expression slightly underestimates the magnitude of $\alpha_{\bar{n}_{\mathrm{Cr}}}$, since the screening is not ideal. For example, in the asymmetric 2-layer slab, $\beta = -76.4$ fJV^{-1}m^{-1}. Using this value in Eq. (3.5), gives $\alpha_{\bar{n}_{\mathrm{Cr}}} = 17.3$ meV, whereas the actual value is $\alpha_{\bar{n}_{\mathrm{Cr}}} = 19.7$ meV. This relationship between $\alpha_{\bar{n}_{\mathrm{Cr}}}$ and β assumes that the slab terminates with a magnetic layer adjacent to the dielectric, and the one term specific to CrSb comes from the ratio $N_l^{\mathrm{Cr}}/N_{\mathrm{u.c.}}$ that was explicitly evaluated to give the factor of 2 in Eq. (3.5). This provides a simple relationship between the conventional metric β and the sensitivity of the MAE to the underlying driving mechanism of sublattice filling.

3.4 Summary and Conclusions

The effects of strain, band filling, and electric field on the MAE of bulk and thin-film CrSb are determined and analysed. A new metric that describes the sensitivity of the MAE to the filling of the magnetic sublattice provides a means to compare the effects of electric field and band filling on the MAE. The magnitude of the bulk magnetostriction coefficient is comparable with those from other antiferromagnets and ferromagnets, however the MAE is large (1.2 meV/u.c.) and its sign cannot be changed by strain for bulk material. For bulk CrSb, depleting the electron density by 0.75 electrons per unit cell depletes the flat, nearly-degenerate d-orbital bands near the Fermi energy and causes a 90° rotation of the Néel vector from out-of-plane to in-plane. Due to the significant ionic nature of the Cr-Sb bond, finite slabs are strongly affected by end termination. Truncation of the bulk

crystal to a thin film consisting of an even number of unit cells, such that one face is a Cr layer and the opposing face is an Sb layer, breaks inversion symmetry, creates a large charge dipole and potential difference across the slab, and breaks spin degeneracy such that the CrSb slab becomes a ferrimagnet. For the 1.1 nm (1.6 nm) slab, the MAE is reduced from 1.2 meV/u.c. to 0.079 meV/u.c. (0.58 meV/u.c) and the strain coefficient is increased from 0.013 meV/%strain to 0.068 meV/%strain (0.062 meV/%strain). As a result of the reduced MAE and increased strain coefficient, the sign of the MAE in the 1.1 nm slab can be switched with 1.5% uniaxial compressive strain. The large SOC from the Sb combined with broken inversion symmetry of the thin film results in an intrinsic VCMA. The calculated VCMA coefficients for the free-standing 1.1 nm and 1.6 nm thin films with vacuum as the insulator are -76.4 fJV^{-1}m^{-1} and -55.3 fJV^{-1}m^{-1}, respectively. If the CrSb slab is terminated with Cr layers on both faces, then it remains a compensated AFM, but with the compensation occurring nonlocally between mirror symmetric Cr pairs. The MAE changes sign so that in-plane alignment of the moments is preferred, the magnitude of the MAE remains large similar to that of the bulk, and it is relatively insensitive to filling. Finally, in a standard experimental configuration, the CrSb slab will have different end terminations with MgO on one face and a HM on the other, so that the FiM state of the asymmetric slab will be the most probable one observed experimentally.

Bibliography

[1] I. J. Park, T. Lee, P. Das, B. Debnath, G. P. Carman, and R. K. Lake. "Strain control of the Néel vector in Mn-based antiferromagnets." *Applied Physics Letters*, **114**(14), 142403 (2019).

[2] I. J. Park, S. Kwon, and R. K. Lake. "Effects of filling, strain, and electric field on the Néel vector in antiferromagnetic CrSb." *Physical review B* (in press).

[3] J. Towns, T. Cockerill, M. Dahan, I. Foster, K. Gaither, A. Grimshaw, V. Hazlewood, S. Lathrop, D. Lifka, G. D. Peterson, *et al.*. "Xsede: accelerating scientific discovery." *Computing in Science & Engineering*, **16**(5), 62–74 (2014).

[4] S. Wolf, D. Awschalom, R. Buhrman, J. Daughton, v. S. von Molnár, M. Roukes, A. Y. Chtchelkanova, and D. Treger. "Spintronics: a spin-based electronics vision for the future." *science*, **294**(5546), 1488–1495 (2001).

[5] I. Žutić, J. Fabian, and S. D. Sarma. "Spintronics: Fundamentals and applications." *Reviews of modern physics*, **76**(2), 323 (2004).

[6] M. N. Baibich, J. M. Broto, A. Fert, F. N. Van Dau, F. Petroff, P. Etienne, G. Creuzet, A. Friederich, and J. Chazelas. "Giant magnetoresistance of (001) fe/(001) cr magnetic superlattices." *Physical review letters*, **61**(21), 2472 (1988).

[7] G. Binasch, P. Grünberg, F. Saurenbach, and W. Zinn. "Enhanced magnetoresistance in layered magnetic structures with antiferromagnetic interlayer exchange." *Physical review B*, **39**(7), 4828 (1989).

[8] E. V. Gomonay and V. M. Loktev. "Spintronics of antiferromagnetic systems." *Low Temperature Physics*, **40**(1), 17–35 (2014).

[9] F. Keffer and C. Kittel. "Theory of antiferromagnetic resonance." *Physical Review*, **85**(2), 329 (1952).

[10] T. Jungwirth, X. Marti, P. Wadley, and J. Wunderlich. "Antiferromagnetic spintronics." *Nature Nanotechnology*, **11**(3), 231–241 (2016). URL dx.doi.org/10.1038/nnano.2016.18.

[11] Y. G. Semenov, X.-L. Li, and K. W. Kim. "Currentless reversal of néel vector in antiferromagnets." *Physical Review B*, **95**(1), 014434 (2017).

[12] V. Lopez-Dominguez, H. Almasi, and P. K. Amiri. "Picosecond electric-field-induced switching of antiferromagnets." *Physical Review Applied*, **11**(2), 024019 (2019).

[13] R. Umetsu, Y. Okamoto, M. Miyakawa, K. Sasao, K. Fukamichi, and A. Sakuma. "Very high antiferromagnetic stability of l10-type mnir alloys." *Journal of magnetism and magnetic materials*, **272**, 790–791 (2004).

[14] R. Y. Umetsu, K. Fukamichi, and A. Sakuma. "Electronic structures and magnetic phase stability of $L1_0$ and $B2$-type MnRh equiatomic alloys." *Journal of the Physical Society of Japan*, **76**(10), 104712–104712 (2007).

[15] L. Pál, E. Krén, G. Kádár, P. Szabó, and T. Tarnóczi. "Magnetic Structures and Phase Transformations in Mn-Based CuAu-I Type Alloys." *Journal of Applied Physics*, **39**(2), 538–544 (1968).

[16] W. Takei, D. E. Cox, and G. Shirane. "Magnetic structures in the mnsb-crsb system." *Physical Review*, **129**(5), 2008 (1963).

[17] V. Baltz, A. Manchon, M. Tsoi, T. Moriyama, T. Ono, and Y. Tserkovnyak. "Antiferromagnetic spintronics." *Rev. Mod. Phys.*, **90**, 015005 (2018). URL dx.doi.org/10.1103/RevModPhys.90.015005.

[18] O. Gomonay, T. Jungwirth, and J. Sinova. "Concepts of antiferromagnetic spintronics." *Physica Status Solidi (RRL) Rapid Research Letters*, **11**(4), 1700022 (2017). URL dx.doi.org/abs/10.1002/pssr.201700022.

[19] C. Grezes, F. Ebrahimi, J. G. Alzate, X. Cai, J. A. Katine, J. Langer, B. Ocker, P. K. Amiri, and K. L. Wang. "Ultra-low switching energy and scaling in electric-field-controlled nanoscale magnetic tunnel junctions with high resistance-area product." *Appl. Phys. Lett.*, **108**(1), 012403 (2016). URL dx.doi.org/10.1063/1.4939446.

[20] A. Sakuma. "Electronic structures and magnetism of CuAu-type MnNi and MnGa." *Journal of Magnetism and Magnetic Materials*, **187**(1), 105–112 (1998).

[21] R. Y. Umetsu, K. Fukamichi, and A. Sakuma. "Electrical and calorimetric evidences of a pseudo-gap in antiferromagnetic equiatomic MnPd alloy." *Journal of magnetism and magnetic materials*, **239**(1-3), 530–532 (2002).

[22] R. Y. Umetsu, M. Miyakawa, K. Fukamichi, and A. Sakuma. "Pseudogap in the density of states and the highest Néel temperature of the $L1_0$-type MnIr alloy system." *Physical Review B*, **69**(10), 104411 (2004).

[23] R. Y. Umetsu, K. Fukamichi, and A. Sakuma. "Electrical and magnetic properties, and electronic structures of pseudo-gap-type antiferromagnetic $L1_0$-type MnPt alloys." *Materials transactions*, **47**(1), 2–10 (2006).

[24] J. Wang, Z. Jiang, W. Chen, X. Zhang, and B. Zhou. "The first-principles study of martensitic transformations in MnMe (Me= Rh, Pd) alloys at low temperatures." *Intermetallics*, **34**, 83–88 (2013).

[25] J. Wang, A. Gao, W. Chen, X. D. Zhang, B. Zhou, and Z. Jiang. "The structural, elastic, phonon, thermal and electronic properties of MnX (X= Ni, Pd and Pt) alloys: First-principles calculations." *Journal of Magnetism and Magnetic Materials*, **333**, 93–99 (2013).

[26] P. Wadley, B. Howells, J. Železnỳ, C. Andrews, V. Hills, R. P. Campion, V. Novák, K. Olejník, F. Maccherozzi, S. S. Dhesi, *et al.*. "Electrical switching of an antiferromagnet." *Science*, **351**(6273), 587–590 (2016).

[27] J. Domann, T. Wu, T.-K. Chung, and G. Carman. "Strain-mediated magnetoelectric storage, transmission, and processing: Putting the squeeze on data." *MRS Bulletin*, **43**(11), 848853 (2018).

[28] Z. Q. Liu, H. Chen, J. M. Wang, J. H. Liu, K. Wang, Z. X. Feng, H. Yan, X. R. Wang, C. B. Jiang, J. M. D. Coey, and A. H. MacDonald. "Electrical switching of the topological anomalous hall effect in a non-collinear antiferromagnet above room temperature." *Nature Electronics*, **1**(3), 172–177 (2018). URL https://doi.org/10.1038/s41928-018-0040-1.

[29] A. Barra, J. Domann, K. W. Kim, and G. Carman. "Voltage control of antiferromagnetic phases at near-terahertz frequencies." *Physical Review Applied*, **9**(3), 034017 (2018).

[30] H. Yan, Z. Feng, S. Shang, X. Wang, Z. Hu, J. Wang, Z. Zhu, H. Wang, Z. Chen, H. Hua, *et al.*. "A piezoelectric, strain-controlled antiferromagnetic memory insensitive to magnetic fields." *Nature Nanotechnology*, **14**, 131–136 (2019). URL https://doi.org/10.1038/s41565-018-0339-0.

[31] G. Kresse and J. Hafner. "Ab initio molecular dynamics for liquid metals." *Physical Review B*, **47**(1), 558 (1993).

[32] P. E. Blöchl. "Projector augmented-wave method." *Physical Review B*, **50**(24), 17953 (1994).

[33] J. P. Perdew, K. Burke, and M. Ernzerhof. "Generalized gradient approximation made simple." *Physical Review Letters*, **77**(18), 3865 (1996).

[34] A. K. Biswas, S. Bandyopadhyay, and J. Atulasimha. "Energy-efficient magnetoelastic non-volatile memory." *Applied Physics Letters*, **104**(23), 232403 (2014).

[35] D.-s. Wang, R. Wu, and A. J. Freeman. "First-principles theory of surface magnetocrystalline anisotropy and the diatomic-pair model." *Phys. Rev. B*, **47**, 14932–14947 (1993). URL https://link.aps.org/doi/10.1103/PhysRevB.47.14932.

[36] A. Bur, T. Wu, J. Hockel, C. J. Hsu, H. K. D. Kim, T. K. Chung, K. Wong, K. L. Wang, and G. P. Carman. "Strain-induced magnetization change in patterned ferromagnetic nickel nanostructures." *Journal of Applied Physics*, **109**(12), 123903 (2011).

[37] A. E. Clark, J. B. Restorff, M. Wun-Fogle, T. A. Lograsso, and D. L. Schlagel. "Magnetostrictive properties of body-centered cubic Fe-Ga and Fe-Ga-Al alloys." *IEEE Transactions on Magnetics*, **36**(5), 3238–3240 (2000).

[38] M. K. Panduranga, T. Lee, A. Chavez, S. V. Prikhodko, and G. P. Carman. "Polycrystalline Terfenol-D thin films grown at CMOS compatible temperature." *AIP Advances*, **8**(5), 056404 (2018).

[39] R. C. Hall. "Single crystal anisotropy and magnetostriction constants of several ferromagnetic materials including alloys of NiFe, SiFe, AlFe, CoNi, and CoFe." *Journal of Applied Physics*, **30**(6), 816–819 (1959).

[40] J. Huang, C. Prados, J. E. Evetts, and A. Hernando. "Giant magnetostriction of amorphous Tb_xFe_{1-x} ($0.10 < x < 0.45$) thin films and its correlation with perpendicular anisotropy." *Physical Review B*, **51**(1), 297 (1995).

[41] D. Fritsch and C. Ederer. "First-principles calculation of magnetoelastic coefficients and magnetostriction in the spinel ferrites $CoFe_2O_4$ and $NiFe_2O_4$." *Physical Review B*, **86**(1), 014406 (2012).

[42] J. Nogués and I. K. Schuller. "Exchange bias." *Journal of Magnetism and Magnetic Materials*, **192**(2), 203–232 (1999).

[43] C. C. Chiang, S. Y. Huang, D. Qu, P. H. Wu, and C. L. Chien. "Absence of evidence of electrical switching of the antiferromagnetic néel vector." *Phys. Rev. Lett.*, **123**, 227203 (2019). URL https://link.aps.org/doi/10.1103/PhysRevLett.123.227203.

[44] A. Churikova, D. Bono, B. Neltner, A. Wittmann, L. Scipioni, A. Shepard, T. Newhouse-Illige, J. Greer, and G. S. D. Beach. "Non-magnetic origin of spin hall magnetoresistance-like signals in pt films and epitaxial nio/pt bilayers." *Applied Physics Letters*, **116**(2), 022410 (2020). URL https://doi.org/10.1063/1.5134814.

[45] X. Chen, X. Zhou, R. Cheng, C. Song, J. Zhang, Y. Wu, Y. Ba, H. Li, Y. Sun, Y. You, *et al.*. "Electric field control of néel spin–orbit torque in an antiferromagnet." *Nature materials*, **18**(9), 931–935 (2019).

[46] X. Wang, Z. Feng, P. Qin, H. Yan, X. Zhou, H. Guo, Z. Leng, W. Chen, Q. Jia, Z. Hu, *et al.*. "Integration of the noncollinear antiferromagnetic metal mn3sn onto ferroelectric oxides for electric-field control." *Acta Materialia*, **181**, 537–543 (2019).

[47] D. Boldrin, A. P. Mihai, B. Zou, J. Zemen, R. Thompson, E. Ware, B. V. Neamtu, L. Ghivelder, B. Esser, D. W. McComb, *et al.*. "Giant piezomagnetism in mn3nin." *ACS applied materials & interfaces*, **10**(22), 18863–18868 (2018).

[48] Z. Liu, H. Chen, J. Wang, J. Liu, K. Wang, Z. Feng, H. Yan, X. Wang, C. Jiang, J. Coey, *et al.*. "Electrical switching of the topological anomalous hall effect in a non-collinear antiferromagnet above room temperature." *Nature Electronics*, **1**(3), 172–177 (2018).

[49] C. Feng, Y. Li, L. Wang, Y. Cao, M. Yao, F. Meng, F. Yang, B. Li, K. Wang, and G. Yu. "Giant strain control of antiferromagnetic moment in metallic femn by tuning exchange spring structure." *Advanced Functional Materials*, **30**, 1909708 (2020). URL doi.org/10.1002/adfm.201909708.

[50] C.-G. Duan, J. P. Velev, R. F. Sabirianov, Z. Zhu, J. Chu, S. S. Jaswal, and E. Y. Tsymbal. "Surface magnetoelectric effect in ferromagnetic metal films." *Phys. Rev. Lett.*, **101**, 137201 (2008). URL https://doi.org/10.1103/PhysRevLett.101.137201.

[51] K. Nakamura, R. Shimabukuro, Y. Fujiwara, T. Akiyama, T. Ito, and A. J. Freeman. "Giant modification of the magnetocrystalline anisotropy in transition-metal monolayers by an external electric field." *Phys. Rev. Lett.*, **102**, 187201 (2009). URL https://link.aps.org/doi/10.1103/PhysRevLett.102.187201.

[52] M. K. Niranjan, C.-G. Duan, S. S. Jaswal, and E. Y. Tsymbal. "Electric field effect on magnetization at the fe/mgo(001) interface." *Applied Physics Letters*, **96**(22), 222504 (2010).

[53] P. K. Amiri and K. L. Wang. "Voltage-controlled magnetic anisotropy in spintronic devices." In *Spin*, vol. 2, p. 1240002 (World Scientific, 2012).

[54] J. G. Alzate, P. Khalili Amiri, G. Yu, P. Upadhyaya, J. A. Katine, J. Langer, B. Ocker, I. N. Krivorotov, and K. L. Wang. "Temperature dependence of the voltage-controlled perpendicular anisotropy in nanoscale mgo— cofeb— ta magnetic tunnel junctions." *Applied physics letters*, **104**(11), 112410 (2014).

[55] T. Nozaki, H. Arai, K. Yakushiji, S. Tamaru, H. Kubota, H. Imamura, A. Fukushima, and S. Yuasa. "Magnetization switching assisted by high-frequency-voltage-induced ferromagnetic resonance." *Applied Physics Express*, **7**(7), 073002 (2014).

[56] P. V. Ong, N. Kioussis, D. Odkhuu, P. Khalili Amiri, K. L. Wang, and G. P. Carman. "Giant voltage modulation of magnetic anisotropy in strained heavy metal/magnet/insulator heterostructures." *Phys. Rev. B*, **92**, 020407 (2015). URL doi.org/10.1103/PhysRevB.92.020407.

[57] W. Skowroński, T. Nozaki, D. D. Lam, Y. Shiota, K. Yakushiji, H. Kubota, A. Fukushima, S. Yuasa, and Y. Suzuki. "Underlayer material influence on electric-field controlled perpendicular magnetic anisotropy in cofeb/mgo magnetic tunnel junctions." *Physical Review B*, **91**(18), 184410 (2015).

[58] W. Skowroński, T. Nozaki, Y. Shiota, S. Tamaru, K. Yakushiji, H. Kubota, A. Fukushima, S. Yuasa, and Y. Suzuki. "Perpendicular magnetic anisotropy of ir/-cofeb/mgo trilayer system tuned by electric fields." *Applied Physics Express*, **8**(5), 053003 (2015).

[59] Y. Hibino, T. Koyama, A. Obinata, K. Miwa, S. Ono, and D. Chiba. "Electric field modulation of magnetic anisotropy in perpendicularly magnetized pt/co structure with a pd top layer." *Applied Physics Express*, **8**(11), 113002 (2015).

[60] T. Nozaki, A. Kozioł-Rachwał, W. Skowroński, V. Zayets, Y. Shiota, S. Tamaru, H. Kubota, A. Fukushima, S. Yuasa, and Y. Suzuki. "Large voltage-induced changes in the perpendicular magnetic anisotropy of an mgo-based tunnel junction with an ultrathin fe layer." *Phys. Rev. Applied*, **5**, 044006 (2016). URL https://link.aps.org/doi/10.1103/PhysRevApplied.5.044006.

[61] Y. Shiota, T. Nozaki, S. Tamaru, K. Yakushiji, H. Kubota, A. Fukushima, S. Yuasa, and Y. Suzuki. "Reduction in write error rate of voltage-driven dynamic magnetization switching by improving thermal stability factor." *Applied Physics Letters*, **111**(2), 022408 (2017).

[62] J. Zhang, P. V. Lukashev, S. S. Jaswal, and E. Y. Tsymbal. "Model of orbital populations for voltage-controlled magnetic anisotropy in transition-metal thin films." *Phys. Rev. B*, **96**, 014435 (2017). URL https://link.aps.org/doi/10.1103/PhysRevB.96.014435.

[63] Z. Wen, H. Sukegawa, T. Seki, T. Kubota, K. Takanashi, and S. Mitani. "Voltage control of magnetic anisotropy in epitaxial ru/co 2 feal/mgo heterostructures." *Scientific reports*, **7**, 45026 (2017).

[64] A. Kozioł-Rachwał, T. Nozaki, K. Freindl, J. Korecki, S. Yuasa, and Y. Suzuki. "Enhancement of perpendicular magnetic anisotropy and its electric field-induced change through interface engineering in Cr/Fe/MgO." *Scientific Reports*, **7**(1), 5993 (2017). URL https://doi.org/10.1038/s41598-017-05994-7.

[65] T. Kawabe, K. Yoshikawa, M. Tsujikawa, T. Tsukahara, K. Nawaoka, Y. Kotani, K. Toyoki, M. Goto, M. Suzuki, T. Nakamura, *et al.*. "Electric-field-induced changes of magnetic moments and magnetocrystalline anisotropy in ultrathin cobalt films." *Physical Review B*, **96**(22), 220412 (2017).

[66] X. Li, K. Fitzell, D. Wu, C. T. Karaba, A. Buditama, G. Yu, K. L. Wong, N. Altieri, C. Grezes, N. Kioussis, *et al.*. "Enhancement of voltage-controlled magnetic anisotropy through precise control of mg insertion thickness at cofeb— mgo interface." *Applied Physics Letters*, **110**(5), 052401 (2017).

[67] Y. Kato, H. Yoda, Y. Saito, S. Oikawa, K. Fujii, M. Yoshiki, K. Koi, H. Sugiyama, M. Ishikawa, T. Inokuchi, *et al.*. "Giant voltage-controlled magnetic anisotropy effect in a crystallographically strained cofe system." *Applied Physics Express*, **11**(5), 053007 (2018).

[68] S. Kwon, Q. Sun, F. Mahfouzi, K. L. Wang, P. K. Amiri, and N. Kioussis. "Voltage-controlled magnetic anisotropy in heterostructures with atomically thin heavy metals." *Phys. Rev. Applied*, **12**, 044075 (2019). URL https://link.aps.org/doi/10.1103/PhysRevApplied.12.044075.

[69] S. Kwon, P.-V. Ong, Q. Sun, F. Mahfouzi, X. Li, K. L. Wang, Y. Kato, H. Yoda, P. K. Amiri, and N. Kioussis. "Colossal electric field control of magnetic anisotropy at ferromagnetic interfaces induced by iridium overlayer." *Physical Review B*, **99**(6), 064434 (2019).

[70] T. Nozaki, M. Endo, M. Tsujikawa, T. Yamamoto, T. Nozaki, M. Konoto, H. Ohmori, Y. Higo, H. Kubota, A. Fukushima, *et al.*. "Voltage-controlled magnetic anisotropy in an ultrathin ir-doped fe layer with a cofe termination layer." *APL Materials*, **8**(1), 011108 (2020).

[71] W. Z. Chen, L. N. Jiang, Z. R. Yan, Y. Zhu, C. H. Wan, and X. F. Han. "Origin of the large voltage-controlled magnetic anisotropy in a cr/fe/mgo junction with an ultrathin fe layer: First-principles investigation." *Phys. Rev. B*, **101**, 144434 (2020). URL https://doi.org/10.1103/PhysRevB.101.144434.

[72] S. Miwa, M. Suzuki, M. Tsujikawa, T. Nozaki, T. Nakamura, M. Shirai, S. Yuasa, and Y. Suzuki. "Perpendicular magnetic anisotropy and its electric-field-induced change at metal-dielectric interfaces." *Journal of Physics D: Applied Physics*, **52**(6), 063001 (2018). URL doi.org/10.1088/1361-6463/aaef18.

[73] K. L. Wang, H. Lee, and P. Khalili Amiri. "Magnetoelectric random access memory-based circuit design by using voltage-controlled magnetic anisotropy in magnetic tunnel junctions." *IEEE Transactions on Nanotechnology*, **14**(6), 992–997 (2015).

[74] W. Kang, Y. Ran, Y. Zhang, W. Lv, and W. Zhao. "Modeling and exploration of the voltage-controlled magnetic anisotropy effect for the next-generation low-power and high-speed mram applications." *IEEE Transactions on Nanotechnology*, **16**(3), 387–395 (2017).

[75] W. Kang, Y. Ran, W. Lv, Y. Zhang, and W. Zhao. "High-speed, low-power, magnetic non-volatile flip-flop with voltage-controlled, magnetic anisotropy assistance." *IEEE Magnetics Letters*, **7**, 1–5 (2016).

[76] G. Zheng, S.-H. Ke, M. Miao, J. Kim, R. Ramesh, and N. Kioussis. "Electric field control of magnetization direction across the antiferromagnetic to ferromagnetic transition." *Scientific reports*, **7**(1), 1–9 (2017).

[77] Y. Su, M. Li, J. Zhang, J. Hong, and L. You. "Voltage-controlled magnetic anisotropy in antiferromagnetic l10-mnpt and mnpd thin films." *Journal of Magnetism and Magnetic Materials*, **505**, 166758 (2020).

[78] P.-H. Chang, W. Fang, T. Ozaki, and K. Belashchenko. "Voltage-controlled magnetic anisotropy in antiferromagnetic mgo-capped mnpt films." *arXiv preprint arXiv:2008.03249* (2020).

[79] J. Dijkstra, C. Van Bruggen, C. Haas, and R. de Groot. "Electronic band-structure calculations of some magnetic chromium compounds." *Journal of Physics: Condensed Matter*, **1**(46), 9163–9174 (1989).

[80] T. Ito, H. Ido, and K. Motizuki. "Electronic structure and magnetic properties in crx (xp, as and sb)." *Journal of Magnetism and Magnetic Materials*, **310**(2), e558–e559 (2007). URL doi.org/10.1016/j.jmmm.2006.10.470.

[81] L. Kahal, A. Zaoui, and M. Ferhat. "Magnetic properties of crsb: A first-principle study." *Journal of Applied Physics*, **101**(9), 093912 (2007). URL doi.org/10.1063/1.2732502.

[82] S. Polesya, G. Kuhn, S. Mankovsky, H. Ebert, M. Regus, and W. Bensch. "Structural and magnetic properties of crsb compounds: Nias structure." *Journal of Physics: Condensed Matter*, **24**(3), 036004 (2011). URL doi.org/10.1088/0953-8984/24/3/036004.

[83] Q. L. He, X. Kou, A. J. Grutter, G. Yin, L. Pan, X. Che, Y. Liu, T. Nie, B. Zhang, S. M. Disseler, B. J. Kirby, W. Ratcliff II, Q. Shao, K. Murata, X. Zhu, G. Yu, Y. Fan, M. Montazeri, X. Han, J. A. Borchers, and K. L. Wang. "Tailoring exchange couplings in magnetic topological-insulator/antiferromagnet heterostructures." *Nature Materials*, **16**(1), 94–100 (2017). URL doi.org/10.1038/nmat4783.

[84] Q. L. He, G. Yin, L. Yu, A. J. Grutter, L. Pan, C.-Z. Chen, X. Che, G. Yu, B. Zhang, Q. Shao, A. L. Stern, B. Casas, J. Xia, X. Han, B. J. Kirby, R. K. Lake, K. T. Law, and K. L. Wang. "Topological transitions induced by antiferromagnetism in a thin-film topological insulator." *Phys. Rev. Lett.*, **121**, 096802 (2018). URL https://link.aps.org/doi/10.1103/PhysRevLett.121.096802.

[85] T. Wang, D. Gao, and M. Si. "Tuning the topological surface states in sb2te3/crsb heterostructures by interface spacing." *Japanese Journal of Applied Physics*, **58**(8), 080910 (2019).

[86] A. I. Snow. "Neutron diffraction investigation of the atomic magnetic moment orientation in the antiferromagnetic compound crsb." *Phys. Rev.*, **85**, 365–365 (1952). URL https://link.aps.org/doi/10.1103/PhysRev.85.365.

[87] G. Henkelman, A. Arnaldsson, and H. Jónsson. "A fast and robust algorithm for bader decomposition of charge density." *Computational Materials Science*, **36**(3), 354–360 (2006). URL http://www.sciencedirect.com/science/article/pii/S0927025605001849.

[88] V. Wang, N. Xu, J. C. Liu, G. Tang, and W.-T. Geng. "Vaspkit: A user-friendly interface facilitating high-throughput computing and analysis using vasp code." (2020). 1908.08269.

[89] J. Neugebauer and M. Scheffler. "Adsorbate-substrate and adsorbate-adsorbate interactions of na and k adlayers on al (111)." *Physical Review B*, **46**(24), 16067 (1992).

[90] G. Makov and M. Payne. "Periodic boundary conditions in ab initio calculations." *Physical Review B*, **51**(7), 4014 (1995).

[91] G. Yu, Z. Wang, M. Abolfath-Beygi, C. He, X. Li, K. L. Wong, P. Nordeen, H. Wu, G. P. Carman, X. Han, I. A. Alhomoudi, P. K. Amiri, and K. L. Wang. "Strain-induced modulation of perpendicular magnetic anisotropy in ta/cofeb/mgo structures investigated by ferromagnetic resonance." *Applied Physics Letters*, **106**(7), 072402 (2015).

[92] Z. Charifi, D. Guendouz, H. Baaziz, F. Soyalp, and B. Hamad. "Ab-initio investigations of the structural, electronic, magnetic and mechanical properties of crx (x= as, sb, se, and te) transition metal pnictides and chalcogenides." *Physica Scripta*, **94**(1), 015701 (2018).

[93] See discussion surrounding Eq. (46) of N. Djavid and R. K. Lake, Phys. Rev. B, **102**, 024419 (2020).

[94] H. X. Yang, M. Chshiev, B. Dieny, J. H. Lee, A. Manchon, and K. H. Shin. "First-principles investigation of the very large perpendicular magnetic anisotropy at fe|mgo and co|mgo interfaces." *Phys. Rev. B*, **84**, 054401 (2011). URL https://doi.org/10.1103/PhysRevB.84.054401.

[95] J. Okabayashi, J. W. Koo, H. Sukegawa, S. Mitani, Y. Takagi, and T. Yokoyama. "Perpendicular magnetic anisotropy at the interface between ultrathin fe film and mgo studied by angular-dependent x-ray magnetic circular dichroism." *Applied Physics Letters*, **105**(12), 122408 (2014). URL https://doi.org/10.1063/1.4896290.

[96] "Materials Project." https://materialsproject.org/materials/mp-1670/. Accessed: 2019-02-13.

[97] P. Das. *Material Genomics for Device Applications: Atoms to High-Throughput Ab-Initio Calculations*. Ph.D. thesis, UC Riverside (2018).

Appendix A

Calculated lattice constants, magnetoelastic anisotropy constants, and determination of Young's moduli of MnX alloys

Figure A.1 shows the change in the lattice constants in MnX alloys as a function of applied strain along the a axis. The a lattice parameter is linearly increased and the b and c lattice constants are relaxed. In Fig. A.2, we show the calculated values of K_{me} evaluated at all values of strain and make a linear fit to extract the slope, which is used as the term $\frac{K_{me}}{\varepsilon_{bb}-\varepsilon_{aa}}$ in the Eq. (2) in the main text. As mentioned in the main paper, the Young's moduli were taken from previous results. [24, 25] However, we were unable to find any values for the Young's modulus of MnIr. To calculate the magnetostriction coefficient

for MnIr, we adopted the bulk modulus from the Materials Project [96] and used the the relation $Y(GPa) = 3K(1-2\nu)$ where Y, K, and ν are the Young's modulus, bulk modulus, and Poisson's ratio, respectively.

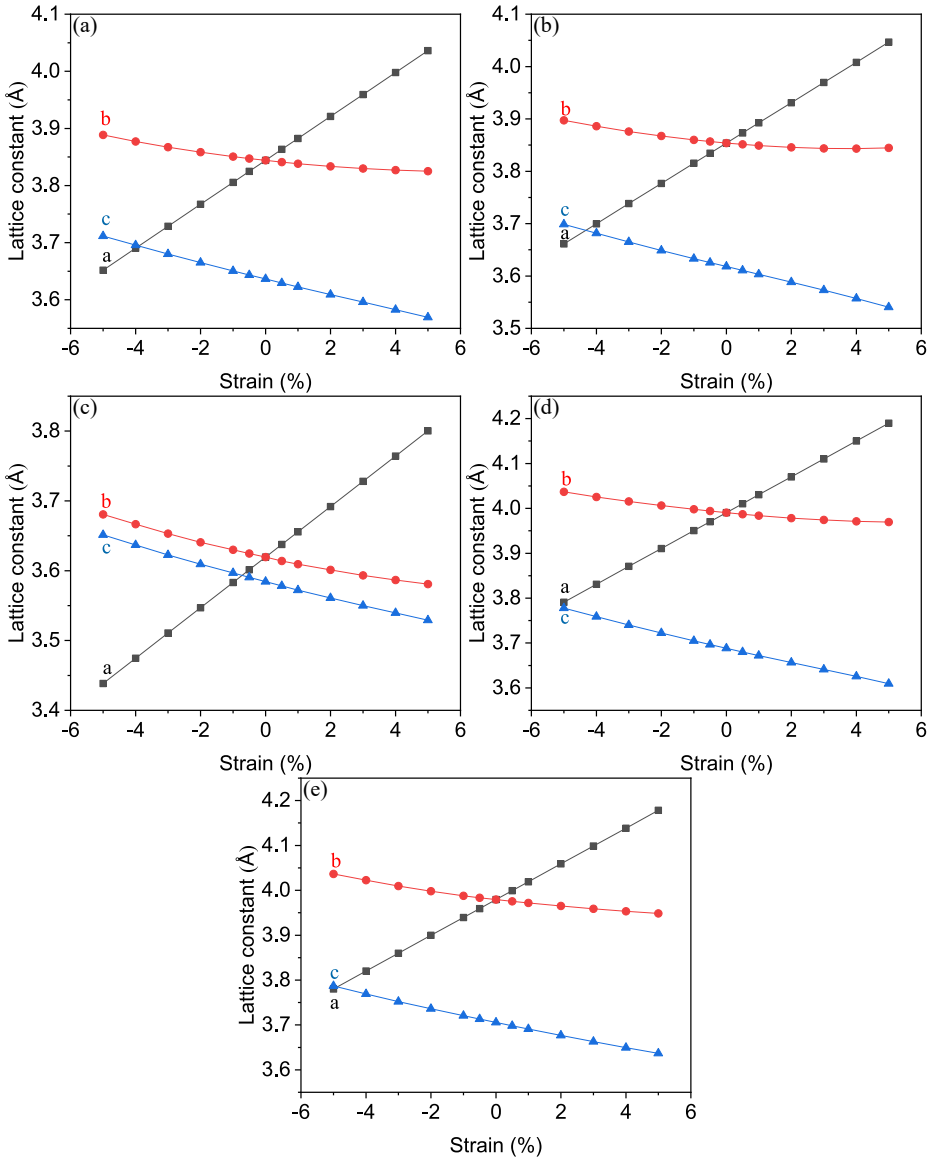

Figure A.1: The lattice constants versus applied strain in (a) MnIr, (b) MnRh, (c) MnNi, (d) MnPd, and (e) MnPt.

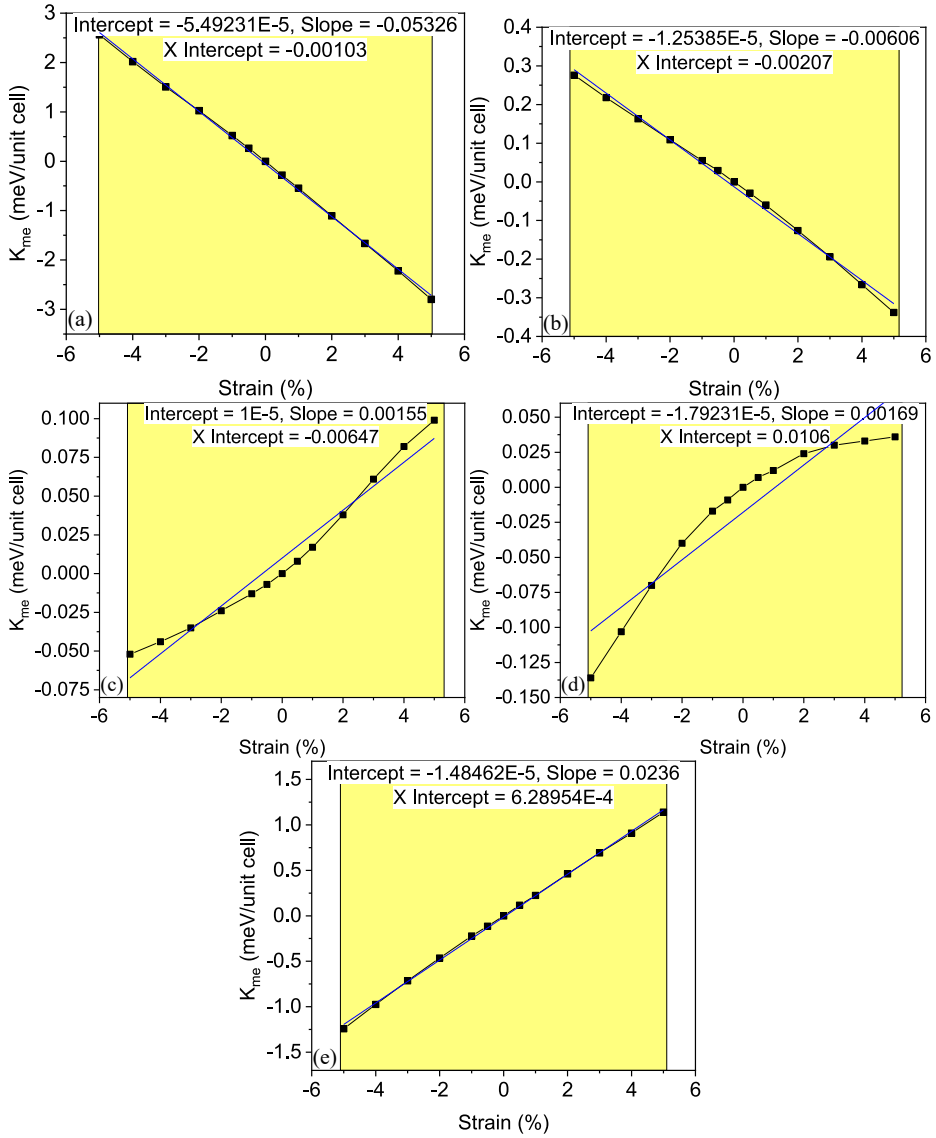

Figure A.2: The magnetoelastic anisotropy constants versus applied strain in (a) MnIr, (b) MnRh, (c) MnNi, (d) MnPd, and (e) MnPt.

Appendix B

Calculation of magnetic anisotropy energy with strain and electric field using ASE package

This section describes how to calculate the magnetic anisotropy energy as a function of applied strain and electric field using atomic simulation environment (ASE) package. Details of the installation of the ASE package and how to use it are discussed in the appendix B of [97]. All the scripts used for calculations are inherrited from [97]. For MAE calculation with respect to the strain, the first step is to apply a strain to the relaxed structure and relax it again. Below is the python script for relaxation.

```
import numpy as np
import ase.io.vasp as vp
from ase.io import *
```

```
from ase.calculators.vasp import Vasp
from shutil import *
from os import path, remove, makedirs
from ase.optimize import BFGS as bfgs
from ase.constraints import UnitCellFilter as ucf
from ase.io.trajectory import Trajectory
np.set_printoptions(precision=2)
# name of input structure
ins_poscar='ase_Cr2Sb2_vol_relaxed.vasp'
# strain inputs (in %)
min_strain = -2.00
max_strain = 2.00
num_strains= 5
# initial magnetic moments
mom=6
u_val=0.25
# mask for unit cell relaxation
# Below, relaxation condition is bi-axial.
mask = [False,True,True,False,False,False]
# force threshold on atoms
fmax = 0.001
isif_dir='0.isif'
```

```
# LDA+U parameters
ldau_param={'Cr':{'L':2, 'U':u_val, 'J':0.0},
            'Sb':{'L':-1, 'U':0.0, 'J':0.0},
           }
# maximum number of steps for the minimizer
steps = 150
# converged kpoints for the structure
kpt=8
# minimizer log file
logfile = 'relax.log'
if not path.exists(isif_dir):
    makedirs(isif_dir)
strains = np.linspace(min_strain/100, max_strain/100, num_strains,
                      endpoint=True)
ins= vp.read_vasp(ins_poscar)
for strain in strains:
    strain_perc = strain*100
    traj_str = 'traj_{:.2f}.traj'.format(strain_perc)
    # vasp parameters
    calc = Vasp(prec = 'Accurate',
            pp = 'pbe',
            istart=0,
```

```
            ismear=0,
            sigma=0.05,
            lcharg=False,
            lwave=False,
            lreal = False,
            lorbit=11,
            ncore = 16,
            ispin=2,
            encut = 500,
            algo='Normal',
            nelm=200,
            ldau=True,
            ldautype=2,
            ldau_luj=ldau_param,
            ediff=1e-7,
            ibrion=-1,
            nsw=0,
            nelmin=4,
            ediffg=-0.01,
            kpts = [kpt,kpt,kpt],
            gamma=True)
    if path.isfile(logfile):
```

```
        remove(logfile)
# Generate cell configurations
    in2 = ins.copy()
    cell_in2 = in2.get_cell()
    strained_cell = cell_in2.copy()
# Here, strain is applied along x-direction.
    strained_cell[:,:1] = cell_in2[:,:1] * (1+strain)
    in2.set_cell(strained_cell, scale_atoms=True)
    initial_vol = in2.get_volume()
# set magnetic moments
    magmom=np.zeros(len(in2))
    cr_ind=0
    for idx, atom in enumerate(in2):
        if atom.symbol == 'Cr' and cr_ind==0 :
            magmom[idx] = mom
            cr_ind= cr_ind + 1
        elif atom.symbol == 'Cr' and cr_ind==1 :
            magmom[idx] = -mom
            break
    calc.set(magmom=magmom)
    in2.set_calculator(calc)
    sf = ucf(in2,mask=mask)
```

```
    bfg = bfgs(sf, logfile=logfile)
    traj = Trajectory(traj_str, 'w', in2)
    bfg.attach(traj)
    bfg.run(fmax=fmax, steps=steps)
    final_vol = in2.get_volume()
    label_str = 'volume relaxed with {:.2f}% strain'
.format(strain_perc)
    poscar_name = 'CONTCAR_{:.2f}.vasp'.format(strain_perc)
    poscar_path = path.join(isif_dir, poscar_name)
    vp.write_vasp(poscar_path, in2, label=label_str,
                  direct=True, sort=True, vasp5=True)
    traj_path = path.join(isif_dir, traj_str)
    copyfile(traj_str, traj_path)
    remove(traj_str)
    log_cpy='relax_{:0.2f}.log'.format(strain_perc)
    log_path = path.join(isif_dir, log_cpy)
    copyfile(logfile, log_path)
    calc.clean()
```

Listing B.1: Script for strain and relaxation

Once the relaxation process is completed, then the next step is to calculate charge density from each strained structure as shown below.

```
import ase.io.vasp as vp
from ase.calculators.vasp import Vasp
from os import path, makedirs, rename, remove
from shutil import *
import subprocess
import numpy as np
conv_kpt=[8, 8, 8]
# strain inputs (in %)
min_strain = -2.00
max_strain = 2.00
num_strains= 5
isif_dir='0.isif'
scf_dir='1.scf'
# initial moment
mag=6
u_val=0.25
ldau_param={'Cr':{'L':2, 'U':u_val, 'J':0.0},
            'Sb':{'L':-1, 'U':0.0, 'J':0.0},
           }
if not path.exists(scf_dir):
    makedirs(scf_dir)
if path.islink('CHGCAR') or path.isfile('CHGCAR'):
```

```
    remove('CHGCAR')
strains = np.linspace(min_strain/100, max_strain/100, num_strains,
                      endpoint=True)
for strain in strains:
    strain_perc = strain * 100
    print('␣Running␣for␣{:.2f}%␣strain...␣'.format(strain_perc),
          end='')
    calc = Vasp(prec = 'Accurate',
            pp = 'pbe',
            istart=0,
            ismear=0,
            sigma=0.05,
            lcharg=True,
            lwave=False,
            lreal=False,
            isym=0, #important to set as zero
            ncore = 16,
            lorbit=11,
            ispin=2,
            encut = 500,
            algo='Normal',
            nelm=200,
```

```
            ldau=True,
            ldautype=2,
            ldau_luj=ldau_param,
            ediff=1e-7,
            ibrion=-1,
            nsw=0,
            nelmin=4,
            isif=3,
            ediffg=-0.001,
            kpts = conv_kpt,
            gamma=True)
poscar_name = 'CONTCAR_{:.2f}.vasp'.format(strain_perc)
poscar_path=path.join(isif_dir, poscar_name)
ins=vp.read_vasp(poscar_path)
in2 = ins.copy()
# set magnetic moments
magmom=np.zeros(len(in2))
cr_ind=0
for idx, atom in enumerate(in2):
    if atom.symbol == 'Cr' and cr_ind==0 :
        magmom[idx] = mag
        cr_ind= cr_ind + 1
```

```
        elif atom.symbol == 'Cr' and cr_ind==1 :
            magmom[idx] = -mag
            break
    calc.set(magmom=magmom)
    in2.set_calculator(calc)
    energy = in2.get_potential_energy()
    fpath1='{}/OSZICAR_{:.2f}'.format(scf_dir, strain_perc)
    rename('OSZICAR',fpath1)
    fpath2 ='{}/OUTCAR_{:.2f}'.format(scf_dir, strain_perc)
    rename('OUTCAR',fpath2)
    fpath3 ='{}/CHGCAR_{:.2f}'.format(scf_dir, strain_perc)
    rename('CHGCAR',fpath3)
```

Listing B.2: Script for charge density calculation

For each strain, OSZICAR, OUTCAR, and CHGCAR files will be saved under '1.scf' folder after this step. Finally, the total energies for different Néel vector directions including spin orbit coupling can be calculated using the script below.

```
import ase.io.vasp as vp
from ase.calculators.vasp import Vasp
from os import path, makedirs, rename, remove
from shutil import *
import subprocess
```

```
import numpy as np

kpt=16

# strain inputs (in %)

min_strain = -2.00

max_strain = 2.00

num_strains= 5

# initial moment

mm_val=6

dir_str='z'

parallel_flag=False

u_val=0.25

ldau_param={'Cr':{'L':2, 'U':u_val, 'J':0.0},

            'Sb':{'L':-1, 'U':0.0, 'J':0.0},

           }

isif_dir='0.isif'

scf_dir='1.scf'

soc_scf_dir='2.ez.axis'

out_summary='summary_strain.txt'

saxis_lst = [[1,0,0],

             [0,0,1],

            ]

if not path.exists(soc_scf_dir):
```

```
    makedirs(soc_scf_dir)
if not path.isfile(out_summary):
    fl=open(out_summary,'w')
    fl.write('{:>8} {:>10} {:>10} \n'
             .format('Strain (%)','S-axis', 'Energy (eV)'))
    fl.flush()
else:
    fl=open(out_summary,'a')
if path.islink('CHGCAR') or path.isfile('CHGCAR'):
    remove('CHGCAR')
strains = np.linspace(min_strain/100, max_strain/100, num_strains,
                      endpoint=True)
for strain in strains:
    strain_perc = strain * 100
    for saxs in saxis_lst:
        calc = Vasp(prec = 'Accurate',
                pp = 'pbe',
                istart=0,
                ismear=0,
                sigma=0.05,
                lwave=False,
                lreal = False,
```

```
                lcharg=True,
                isym=0,
                encut = 500,
                algo='Normal',
                ldau=True,
                ldautype=2,
                ldau_luj=ldau_param,
                ibrion=-1,
                nsw=0,
                nelmin=4,
                isif=3,
                ediffg=-0.001,
                icharg=11,
                ncore=16,
                lsorbit=True,
                gga_compat=False,
                ediff=1e-7,
                lorbit=11,
                kpts = [kpt, kpt, kpt],
                gamma=True)
        poscar_name = 'CONTCAR_{:.2f}.vasp'.format(strain_perc)
        calc.string_params.update({'saxis':'{} {} {}'.format
```

```
                                    (saxs[0],saxs[1],saxs[2])})
    poscar_path=path.join(isif_dir , poscar_name)
    chgcar_dir= '{}/CHGCAR_{:.2f}'.format(scf_dir ,
                                          strain_perc)
    copyfile(chgcar_dir,'CHGCAR')
    in2=vp.read_vasp(poscar_path)
    in2.set_calculator(calc)
    energy = in2.get_potential_energy()
    saxis_str = '{}{}{}'.format(saxs[0], saxs[1], saxs[2])
    fl.write('{:6.2f} {} {:7.6f}\n'.format(strain_perc ,
                                           saxis_str , energy))
    fpath1 ='{}/OSZICAR_{}_{:.2f}'.format(soc_scf_dir ,
                                          saxis_str ,
                                          strain_perc)
    rename('OSZICAR',fpath1)
    fpath2 ='{}/OUTCAR_{}_{:.2f}'.format(soc_scf_dir ,
                                         saxis_str ,
                                         strain_perc)
    rename('OUTCAR',fpath2)
    fpath3 ='{}/CHGCAR_{}_{:.2f}'.format(soc_scf_dir ,
                                         saxis_str ,
                                         strain_perc)
```

```
            rename('CHGCAR',fpath3)
            fl.flush()
        calc.clean()
fl.close()
```

Listing B.3: Script for total energies calculations with different Néel vector orientations

After the script finishes running, OSZICAR, OUTCAR, and CHGCAR files will be saved under '2.ez.axis' folder. For summarizing results, the values of strain, directions of Néel vector, and the corresponding total energies will be recorded in 'summary_strain.txt' file as follows

```
Strain (%)     S-axis Energy (eV)
 -2.00 100 -26.794439
 -2.00 001 -26.795599
 -1.00 100 -26.802454
 -1.00 001 -26.803662
  0.00 100 -26.806066
  0.00 001 -26.807287
  1.00 100 -26.804936
  1.00 001 -26.806170
  2.00 100 -26.798950
  2.00 001 -26.800214
```

To calculate the MAE as a function of electric field in thin films, creating a slab geometry is the first step. It can be done by using a visualization software or writing a python script as below.

```
import ase.io.vasp as vp
bulk = vp.read_vasp('CrSb_bulk.vasp')
surface = bulk.copy()
slab = surface * (1, 1, 2)
slab.center(vacuum=15.0, axis=2)
vp.write_vasp('CrSb_2L.vasp', slab, direct=False, sort=True,
              vasp5=True)
```

Listing B.4: Python scirpt for creating a slab

The next step is to relax the slab geometry with the dipole correction as below.

```
import numpy as np
import ase.io.vasp as vp
from ase.io import *
from ase.calculators.vasp import Vasp
from shutil import *
from os import path, remove, makedirs, rename
np.set_printoptions(precision=2)
# name of input structure
ins_poscar='CrSb_2L.vasp'
```

```
# strain inputs (in %)
min_strain =  0.00
max_strain =  0.00
num_strains=1
# initial magnetic moments
mom=6
def_mom=0
u_val=0.25
isif_dir='0.isif'
# LDA+U parameters
ldau_param={'Cr':{'L':2, 'U':u_val, 'J':0.0},
            'Sb':{'L':-1, 'U':0.0, 'J':0.0},
           }
# converged kpoints for the structure
kpt=23
if not path.exists(isif_dir):
    makedirs(isif_dir)
strains = np.linspace(min_strain/100, max_strain/100, num_strains,
                      endpoint=True)
ins= vp.read_vasp(ins_poscar)
for strain in strains:
    strain_perc = strain*100
```

```
# vasp parameters
calc = Vasp(prec = 'Accurate',
            pp = 'pbe',
            istart=0,
            ismear=0,
            sigma=0.05,
            lcharg=True,
            lwave=False,
            ncore = 16,
            idipol=3,
            ldipol=True,
            ispin=2,
            encut = 500,
            algo='Normal',
            ediff=1e-7,
            ibrion=2,
            nelm=700,
            ldau=True,
            ldautype=2,
            ldau_luj=ldau_param,
            nsw=200,
            isif=4,
```

```
            nelmin=4,
            ediffg=-0.001,
            kpts = [kpt,kpt,1],
            gamma=True)
# Generate cell configurations
in2 = ins.copy()
cell_in2 = in2.get_cell()
strained_cell = cell_in2.copy()
strained_cell[:,:1] = cell_in2[:,:1] * (1+strain)
in2.set_cell(strained_cell, scale_atoms=True)
initial_vol = in2.get_volume()
# set magnetic moments
magmom=np.zeros(len(in2))
cr_ind=0
for idx, atom in enumerate(in2):
    if atom.symbol == 'Cr' and cr_ind==0 :
        magmom[idx] = mom
        cr_ind= cr_ind + 1
    elif atom.symbol == 'Cr' and cr_ind==1 :
        magmom[idx] = mom
        cr_ind= cr_ind + 1
    elif atom.symbol == 'Cr' and cr_ind==2 :
```

```
                magmom[idx] = -mom
                cr_ind= cr_ind + 1
            elif atom.symbol == 'Cr' and cr_ind==3 :
                magmom[idx] = -mom
                break
    calc.set(magmom=magmom)
    in2.set_calculator(calc)
    energy = in2.get_potential_energy()
    fpath1 = '{}/CONTCAR_{:.2f}.out'.format(isif_dir ,
                                            strain_perc)
    copyfile('CONTCAR',fpath1)
    fpath2 ='{}/OSZICAR_{:.2f}'.format(isif_dir , strain_perc)
    rename('OSZICAR',fpath2)
calc.clean()
```

Listing B.5: Strain and relaxation for the slab structure

Here, strain is still included since it might be useful for the future study on strain-meditated VCMA. If strain is included, one of the vasp parameters, isif, should be set as 2, and the strain should be applied to the relaxed structure by the script above. Once the relaxed structure is obtained, the charge density needs to be calculated without electric field. The python scipt for this step is below.

```
import ase.io.vasp as vp
```

```
from ase.calculators.vasp import Vasp
from os import path, makedirs, rename, remove
from shutil import *
import subprocess
import numpy as np
conv_kpt=[23, 23, 1]
# strain inputs (in %)
min_strain = 0.00
max_strain = 0.00
num_strains= 1
# initial moment
mag=6
def_mom=0
u_val=0.25
ldau_param={'Cr':{'L':2, 'U':u_val, 'J':0.0},
            'Sb':{'L':-1, 'U':0.0, 'J':0.0},
           }
isif_dir='0.isif'
scf_dir='1.scf'
if not path.exists(scf_dir):
    makedirs(scf_dir)
if path.islink('CHGCAR') or path.isfile('CHGCAR'):
```

```
    remove('CHGCAR')
strains = np.linspace(min_strain/100, max_strain/100, num_strains,
                      endpoint=True)
for strain in strains:
    strain_perc = strain * 100
    calc = Vasp(prec = 'Accurate',
            pp = 'pbe',
            istart=0,
            ismear=0,
            sigma=0.05,
            lcharg=True,
            lwave=False,
            isym=0,
            ncore = 16,
            lorbit=11,
            idipol=3,
            ldipol=True,
            ispin=2,
            encut = 500,
            algo='Normal',
            ediff=1e-7,
            ibrion=-1,
```

```
            nelm=700,
            ldau=True,
            ldautype=2,
            ldau_luj=ldau_param,
            nsw=0,
            kpts = conv_kpt,
            gamma=True)
    poscar_name = 'CONTCAR_{:.2f}.vasp'.format(strain_perc)
    poscar_path=path.join(isif_dir, poscar_name)
    ins=vp.read_vasp(poscar_path)
    in2 = ins.copy()
    # set magnetic moments
    magmom=np.zeros(len(in2))
    cr_ind=0
    for idx, atom in enumerate(in2):
        if atom.symbol == 'Cr' and cr_ind==0 :
            magmom[idx] = mag
            cr_ind= cr_ind + 1
        elif atom.symbol == 'Cr' and cr_ind==1 :
            magmom[idx] = mag
            cr_ind= cr_ind + 1
        elif atom.symbol == 'Cr' and cr_ind==2 :
```

```
                magmom[idx] = -mag
                cr_ind= cr_ind + 1
            elif atom.symbol == 'Cr' and cr_ind==3 :
                magmom[idx] = -mag
                break
    calc.set(magmom=magmom)
    in2.set_calculator(calc)
    energy = in2.get_potential_energy()
    fpath1 ='{}/OSZICAR_{:.2f}'.format(scf_dir, strain_perc)
    rename('OSZICAR',fpath1)
    fpath2 ='{}/OUTCAR_{:.2f}'.format(scf_dir, strain_perc)
    rename('OUTCAR',fpath2)
    fpath3 ='{}/CHGCAR_{:.2f}'.format(scf_dir, strain_perc)
    rename('CHGCAR',fpath3)
calc.clean()
```

Listing B.6: Script for charge density calculation of the slab

After the charge density calculation, the charge density has to be relaxed with different electric fields. To do it, another self-consistent calculation is required. In this step, icharg has to be set as 1 to read the CHGCAR file from the previous step and the electric field is set by using efield tag as shown below.

```
import ase.io.vasp as vp
```

```
from ase.calculators.vasp import Vasp
from os import path, makedirs, rename, remove
from shutil import *
import subprocess
import numpy as np
conv_kpt=[23, 23, 1]
# field inputs (in eV/A)
min_field = 0.0
max_field = 0.0
num_fields= 1
mag=4
u_val=0.25
ldau_param={'Cr':{'L':2, 'U':u_val, 'J':0.0},
            'Sb':{'L':-1, 'U':0.0, 'J':0.0},
           }
isif_dir='0.isif'
scf_dir='1.scf'
scf_field_dir='2.scf_field'
if not path.exists(scf_field_dir):
    makedirs(scf_field_dir)
if path.islink('CHGCAR') or path.isfile('CHGCAR'):
    remove('CHGCAR')
```

```
fields = np.linspace(min_field, max_field, num_fields,
                     endpoint=True)
for field in fields:
    calc = Vasp(prec = 'Accurate',
                pp = 'pbe',
                istart=0,
                ismear=0,
                sigma=0.05,
                lcharg=True,
                lwave=False,
                isym=0,
                ncore = 16,
                lorbit=11,
                idipol=3,
                ldipol=True,
                lvhar=True,
                efield=field,
                icharg=1,
                ispin=2,
                encut = 500,
                algo='Normal',
                ediff=1e-7,
```

```
            ibrion=-1,
            nelm=700,
            ldau=True,
            ldautype=2,
            ldau_luj=ldau_param,
            nsw=0,
            ediffg=-0.001,
            kpts = conv_kpt,
            gamma=True)
#POSCAR(CHGCAR) name='CONTCAR(CHGCAR)_strain'#
    poscar_name = 'CONTCAR_0.00.vasp'
    poscar_path=path.join(isif_dir, poscar_name)
    chgcar_dir= '{}/CHGCAR_0.00'.format(scf_dir)
    copyfile(chgcar_dir,'CHGCAR')
    ins=vp.read_vasp(poscar_path)
    in2 = ins.copy()
    magmom=np.zeros(len(in2))
    cr_ind=0
    for idx, atom in enumerate(in2):
        if atom.symbol == 'Cr' and cr_ind==0 :
            magmom[idx] = mag
            cr_ind= cr_ind + 1
```

```
        elif atom.symbol == 'Cr' and cr_ind==1 :
            magmom[idx] = mag
            cr_ind= cr_ind + 1
        elif atom.symbol == 'Cr' and cr_ind==2 :
            magmom[idx] = -mag
            cr_ind= cr_ind + 1
        elif atom.symbol == 'Cr' and cr_ind==3 :
            magmom[idx] = -mag
            break
    calc.set(magmom=magmom)
    in2.set_calculator(calc)
    energy = in2.get_potential_energy()
    fpath1 ='{}/OSZICAR_{:.2f}'.format(scf_field_dir, field)
    rename('OSZICAR',fpath1)
    fpath2 ='{}/OUTCAR_{:.2f}'.format(scf_field_dir, field)
    rename('OUTCAR',fpath2)
    fpath3 ='{}/CHGCAR_{:.2f}'.format(scf_field_dir, field)
    rename('CHGCAR',fpath3)
calc.clean()
```

Listing B.7: Script for charge relaxation with electric field

Finally, the total energies with different orientations of Néel vector as a function of electric field can be calculated by running the following python script.

```
import ase.io.vasp as vp
from ase.calculators.vasp import Vasp
from os import path, makedirs, rename, remove
from shutil import *
import subprocess
import numpy as np
conv_kpt=[46, 46, 1]
# field inputs (in eV/A)
import ase.io.vasp as vp
from ase.calculators.vasp import Vasp
from os import path, makedirs, rename, remove
from shutil import *
import subprocess
import numpy as np
conv_kpt=[46, 46, 1]
# field inputs (in eV/A)
min_field = 0.00
max_field = 0.00
num_fields= 1
dir_str='z'
parallel_flag=False
u_val=0.25
```

```
isif_dir='0.isif'

scf_dir='2.scf_field'

soc_scf_dir='3.ez.axis'

out_summary='summary_strain.txt'

ldau_param={'Cr':{'L':2, 'U':u_val, 'J':0.0},

            'Sb':{'L':-1, 'U':0.0, 'J':0.0},

           }

saxis_lst = [[1,0,0],

             [0,0,1],

            ]

if not path.exists(soc_scf_dir):

    makedirs(soc_scf_dir)

if not path.isfile(out_summary):

    fl=open(out_summary,'w')

    fl.write('{:>8} {:>10} {:>10} \n'

             .format('Efield (eV/A)','S-axis', 'Energy (eV)'))

    fl.flush()

else:

    fl=open(out_summary,'a')

if path.islink('CHGCAR') or path.isfile('CHGCAR'):

    remove('CHGCAR')

fields = np.linspace(min_field, max_field, num_fields,
```

```
                    endpoint=True)
for field in fields:
    for saxs in saxis_lst:
        calc = Vasp(prec = 'Accurate',
                pp = 'pbe',
                istart=0,
                ismear=0,
                sigma=0.05,
                lwave=False,
                lcharg=True,
                lreal = False,
                encut = 500,
                idipol=3,
                ldipol=True,
                lvhar=True,
                efield=field,
                algo='Normal',
                icharg=11,
                lorbmom=True,
                ncore=16,
                lsorbit=True,
                nbands=60,
```

```
            isym=0,
            ldau=True,
            ldautype=2,
            ldau_luj=ldau_param,
            gga_compat=False,
            ediff=1e-7,
            lorbit=11,
            kpts = conv_kpt,
            gamma=True)
poscar_name = 'CONTCAR_0.00.vasp'
calc.string_params.update({'saxis':'{} {} {}'.format
                           (saxs[0],saxs[1],saxs[2])})
poscar_path=path.join(isif_dir, poscar_name)
chgcar_dir= '{}/CHGCAR_{:.2f}'.format(scf_dir, field)
copyfile(chgcar_dir,'CHGCAR')
in2=vp.read_vasp(poscar_path)
in2.set_calculator(calc)
energy = in2.get_potential_energy()
saxis_str = '{}{}{}'.format(saxs[0], saxs[1], saxs[2])
fl.write('{:6.2f} {} {:7.6f}\n'
         .format(field, saxis_str, energy))
fpath1 ='{}/OSZICAR_{}_{:.2f}'.format(soc_scf_dir,
```

```
                                                saxis_str,
                                                field)
            rename('OSZICAR',fpath1)
            fpath2 ='{}/OUTCAR_{}_{:.2f}'.format(soc_scf_dir,
                                                saxis_str,
                                                field)
            rename('OUTCAR',fpath2)
            fpath3 ='{}/CHGCAR_{}_{:.2f}'.format(soc_scf_dir,
                                                saxis_str,
                                                field)
            rename('CHGCAR',fpath3)
            fl.flush()
        calc.clean()
fl.close()
```

Appendix C

Tutorial for the Bader charge and Hartree potential calculation

The Bader charge [87], planar averaged Hartree potential, and charge density are useful for analyzing the charge transfer, potential distribution under electric field. Here, the details of calculations of them will be discussed. The required scripts or progams to analyze them are 'bader', 'chgsum.pl', and 'vaspkit'. These codes are available at http://theory.cm.utexas.edu/henkelman/code/bader/, http://theory.cm.utexas.edu/vtsttools/scripts.html, and https://vaspkit.com/, respectively. The first step for the Bader charge analysis is to relax the structure and get the charge density distribution file (CHGCAR), which can be done by using the python script in the previous appendix. For a bulk structure, bader charge calculation can be done by using the command as follows

```
path1/bader CHGCAR -b weight
```

where 'path1' is the directory that contains executable file 'bader'. After executing the file, it generates three output files named 'ACF.dat', 'BCF.dat', and 'AtomVolumes.dat' Among these files, 'ACF.dat' file contains the information of the coordinates of each atom, the charge on each atom, the volume, and the minimum ditance to the surface. For a slab structure, the procedure is different from the bulk since the vacuum region needs to be included. As the same for bulk, the first step is to perform the self-consistent calculation after the relaxation. In this step, one needs to add the tag 'LAECHG=.TRUE.' in the INCAR file. Once the calculation is done, VASP will write AECCAR0 and AECCAR2 which contain the core charge and valence charge, respectively. After that, to write the total charge from the generated files, execute the following from the command

```
path2/chgsum.pl AECCAR0 AECCAR2
```

where the 'path2' is the full path of the directory where the script is. Finally, the calculation of the Bader charge in a thin film can be done by executing.

```
path1/bader -vac auto CHGCAR -ref CHGCAR_sum
```

The calculations of planar averaged Hartree potential and charge is relatively simpler than the Bader charge calculation. Assuming the relaxed structure is already obtained, the first step is to perform self-consistent calculation with the tag 'LVHAR=.TRUE.' being included in the INCAR file to write the Hartree potential in the LOCPOT file. After that, use the 'vaspkit' [88] to calculate the planar averaged potential and charge from the LOCPOT and CHGCAR files, respectively, by executing the command

```
path3/vaspkit
```

where the path3 is the full path of the directory where the excutable 'vaspkit' is. The code will ask the user to specify the calculation from the command, which is straighfoward to do. Once the user runs the function correctly, the code will gernerate the 'CHGPAVG.dat' file from CHGCAR and 'POTPAVG.dat' from LOCPOT. The 'CHGPAVG.dat' and 'POTPAVG.dat' files contain the planar averaged charge density in units of e and potential in units of eV, respectively. The common information in the files is the planar distance in units of Å.